Global changes in water vapor 1979-2020

Allan, R. P. ORCID: https://orcid.org/0000-0003-0264-9447,
Willett, K. M. ORCID: https://orcid.org/0000-0001-5151-0076,
John, V. O. ORCID: https://orcid.org/0000-0003-3280-978X
and Trent, T. ORCID: https://orcid.org/0000-0001-9215-5808

It is advisable to refer to the publisher's version if you intend to cite from the
work. See Guidance on citing.

www.reading.ac.uk/centaur

CentAUR

Global Changes in Water Vapor 1979–2020

Richard P. Allan[1], **Kate M. Willett[2]**, **Viju O. John[3]**, and **Tim Trent[4]**

[1]Department of Meteorology, National Centre for Earth Observations, University of Reading, Reading, UK, [2]Met Office Hadley Centre, Exeter, UK, [3]EUMETSAT, Darmstadt, Germany, [4]School of Physics and Astronomy, National Centre for Earth Observation, University of Leicester, Leicester, UK

Abstract Global-scale changes in water vapor and responses to surface temperature variability since 1979 are evaluated across a range of satellite and ground-based observations, a reanalysis (ERA5) and coupled and atmosphere-only CMIP6 climate model simulations. Global-mean column integrated water vapor increased by 1%/decade during 1988–2014 in observations and atmosphere-only simulations. However, coupled simulations overestimate water vapor trends and this is partly explained by past studies showing that internal climate variability suppressed observed warming in this period. Decreases in low-altitude tropical water vapor in ERA5 and ground-based observations before around 1993 are considered suspect based on inconsistency with simulations and increased column integrated water vapor in microwave satellite data since 1979. Atmospheric Infra-red Sounder satellite data does not capture the increased tropospheric water vapor since 2002 shown by other satellite, reanalysis, and model products. However, global water vapor responses to interannual surface temperature variability are consistent across data sets with increases of ~4%–5% near the surface and 10%–15% at 300 hPa for each 1°C increase in global surface temperature. Global water vapor responses are explained by thermodynamic amplification of upper tropospheric temperature changes and the Clausius Clapeyron temperature dependence of saturation vapor pressure that are dominated by the tropical ocean responses. Upper tropospheric moistening is larger in climate model simulations with greater upper tropospheric warming.

Plain Language Summary Evaporated water becomes a gas (water vapor) in the air where it traps heat by absorbing thermal infrared radiative energy as well as sunlight. Water vapor is also the "fuel" for rain and snowfall. As the climate warms, water vapor increases in the lowest few kilometers of the atmosphere, therefore, causes greater trapping of heat but also heavier precipitation events. This study looks at how water vapor has changed since 1979 by examining satellite measurements, observations at ground level and complex computer simulations that are also used to make predictions of future climate change. We find that the total water vapor in the atmosphere is increasing by about 1% every 10 years. Changes calculated as a percentage of the initial amount are larger higher up in the atmosphere, which is consistent with simple physics. There are some differences between the observations and simulations: some simulations overestimate the observed changes and this is partly because natural fluctuations in the ocean temporarily slowed the warming over the period studied (1988–2014). It is not known for sure what other differences between observations are caused by but it seems possible that decreases in humidity in some data sets may not be real and we are confident that water vapor is increasing with warming of climate.

1. Introduction

Water vapor increases the magnitude of climate change in response to natural and human-caused climate variability and change through a powerful amplifying feedback (Dessler et al., 2008; Forster et al., 2021; Manabe & Wetherald, 1967; Soden et al., 2002, 2005). This is determined by thermodynamically driven increases in water vapor with temperature that cause greater longwave and shortwave radiative absorption by the atmosphere. Increases in low-altitude water vapor with warming are also central in water cycle intensification, including heavy precipitation and associated flood events (Allan & Soden, 2008; Douville et al., 2021; Fowler et al., 2021).

The water vapor feedback is physically well understood and there is good agreement in its magnitude between observations (1.85 ± 0.32 Wm^{-2}K^{-1}) and climate model simulations (1.77 ± 0.20 Wm^{-2}K^{-1}; Forster et al., 2021), yet there remains some uncertainty in altitude dependent changes that in part relate to the pattern of warming, temperature lapse rate responses as well as atmospheric and surface processes (Allan et al., 2002; Colman & Soden, 2021; Dessler et al., 2013; Forster et al., 2021). Although humidity distributions are improved in higher resolution, storm-resolving models, a substantial range remains in some dynamical regimes such as

during transition between moist convection and suppressed phases and very dry regions of strong subsidence (Lang et al., 2021). Notable discrepancies also exist in low-altitude humidity changes in recent decades (Dunn et al., 2017; Simmons et al., 2010; Willett et al., 2020). While it is not yet clear to what extent discrepancies relate to inhomogeneity in data records, spatial sampling, or physical inadequacies in the model simulations (Douville et al., 2021), it remains important to evaluate height-dependent variability in water vapor across observing systems and model simulations. For example, using this approach, Santer et al. (2021) demonstrated a strong relationship between trends in column integrated water vapor and surface temperature and argue that microwave satellite-based lower tropospheric temperature trends are underestimated based upon multiple lines of evidence using a range of climate models, observations, and reanalyses. Thus, the motivation of the present study is to assess consistencies and discrepancies across multiple satellite and ground-based observations, global reanalysis estimates and the latest climate model simulations from Phase 6 of the Coupled Model Intercomparison Project (CMIP6; Eyring et al., 2016). While evaluation of CMIP6 simulations at the regional scale are ongoing (e.g., He et al., 2022), here the objective is to assess global-scale tropospheric water vapor and temperature changes and responses to surface temperature temporal variability over the 40 yr period since 1979 from multiple lines of evidence.

2. Data and Methods

While observational sampling and its variation over time represents a limitation in the observational record (e.g., Schröder et al., 2018; Willett et al., 2020), the goal of the present study is to assess tropical and global mean changes over the satellite era (since 1979) that allows consistent comparison across observations, reanalyses and climate models. To enable this, an imperfect yet pragmatic approach is to employ a set of complimentary, near-global observing systems, covering most of the troposphere, and to merge the incompletely sampled observations with a state of the art reanalysis system. Specific and relative humidity and temperature are assessed, focusing on deseasonalized area mean anomalies which are computed as relative (percentage deviation) from climatological area-mean averages for specific humidity and absolute deviations for temperature (K) and relative humidity (% RH). The troposphere is resolved across seven pressure levels (300, 400, 500, 600, 700, 850, and 925 hPa). Water vapor feedback operating near the tropical tropopause and in the lower stratosphere is not considered due to limitations in the satellite estimates used in the present study, though its importance to the overall feedback is nevertheless acknowledged (Dessler et al., 2013).

2.1. Reanalysis

The fifth generation European Center for Medium-range Weather Forecasts (ECMWF) global reanalysis (ERA5; Hersbach et al., 2020) combines observations with a high-resolution atmosphere modeling system via four dimensional-variational data assimilation. Extensive conventional and satellite observations of surface and tropospheric temperature and humidity are assimilated, including the SSMI(S), Atmospheric Infra-red Sounder (AIRS), HIRS, and MetOp radiance data that are also used to construct the climate data sets used in the present study. ERA5 provides a consistent hourly record of the atmosphere, land, and ocean surface since 1950 using a ~31 km horizontal grid and 137 levels in the vertical. Monthly means of daily means covering the period 1979–2020 are considered: data on a 0.25×0.25 degree latitude-longitude grid are extracted, considering 2 m and pressure level air temperature, column integrated and pressure level specific and relative humidity. Monthly mean near-surface (2 m) specific humidity is computed from monthly 2 m air temperature, dewpoint temperature and surface pressure (Simmons et al., 1999). Computing using monthly rather than hourly fields is not expected to noticeably affect the estimates of deseasonalized trends and variability based on additional calculations (see Supporting Information).

2.2. Observations

2.2.1. AIRS Infrared Satellite Data

The AIRS instrument provides a calibrated, spectrally resolved record of combined infrared and microwave radiances (Tian et al., 2019; Trent et al., 2019) from which temperature and humidity profiles through the troposphere are retrieved in up to 80% cloud cover. Outgoing longwave radiation computed from the retrieved temperature and humidity profiles show consistency with independent satellite measurements (Sun et al., 2011), though

discrepancies relate to sampling and undetected cirrus. Version 6 AIRS data was combined with simulations based on reanalysis inputs to remove systematic biases related to sampling, thereby producing a product suitable for evaluating climate model simulations as part of the Obs4MIP project (version 2: Tian & Hearty, 2020) from September 2002 to September 2016. Given this treatment of systematic biases and the focus of the analysis on variability in anomalies, it is expected that biases due to retrieval errors in regions of substantial or undetected cloud will not substantially affect the results. Since ERA5 provides values by extrapolation for pressure levels below the surface (e.g., mountains), these values are used to fill these missing data areas to ensure sampling consistency, though this only noticeably affects result over land for the 925 hPa level (by <10% for global trends; Figure S2 in Supporting Information S1). Also considered for comparison is the version 7 AIRS-only Level 3 monthly product (an average of the ascending and descending H2OMMR variable) from 2002—present (AIRS Project, 2020) but the focus of the present study is on the AIRS + AMSU v6 Obs4MIP data set (Tian & Hearty, 2020) which is used throughout unless otherwise stated.

2.2.2. Upper Tropospheric Humidity (UTH) Satellite Data

UTH data for 60°S–60°N from two satellite sources are used in this study (John et al., 2021). One is based on infrared radiances measured by the High-Resolution Infrared Radiation Sounder (HIRS; 6.7 to 6.5 μm Channel 12) instruments (Shi & Bates, 2011) and the other is based on the microwave radiances measured by Advanced microwave sounding unit (AMSU-B; 183.31 GHz channels) or Microwave Humidity Sounder (MHS; 190.31 GHz channels) instruments (Chung et al., 2013). In these data sets, UTH represents a Jacobian weighted average of relative humidity with respect to water in a broad layer which is roughly between 500 and 200 hPa, but slightly varies depending upon atmospheric humidity profile with lower altitude layers sampled for drier, higher latitude profiles. Therefore, analysis focuses primarily on tropical regions. John et al. (2021) present the variability and change in UTH in these data sets.

2.2.3. SSMI(S) and SMMR Microwave Satellite Observations

The Special Sensor Microwave Imager (SSM/I) and the Special Sensor Microwave Imager Sounder (SSMIS) are passive microwave radiometers onboard Defense Meteorological Satellite Program satellites since 1987. Column integrated water vapor, retrieved and averaged onto a 0.25 × 0.25 degree grid over the ice-free oceans (Mears et al., 2015; Wentz, 2015), is taken from the Remote Sensing Systems SSM/I records (F08, 1987–1991; F11, 1992–1995; F13, 1996–1999; F15, 2000–2006) and the SSMIS record (F17, 2007–2020). These were chosen as the set with a relatively stable satellite overpass time. Also considered was 1 × 1° resolution Scanning Multichannel Microwave Radiometer (SMMR) data over the ice free oceans from 1979 to 1984, also generated by Remote Sensing Systems (Wentz & Francis, 1992) and used in previous assessments of column integrated water vapor changes (e.g., Allan et al., 2003). These records were merged with the ERA5 data by replacing missing data, primarily over land and ice-covered ocean, to provide a globally complete observations-based estimate of column integrated water vapor for 1979–1984 and since July 1987.

2.2.4. HadISDH Ground Based Humidity Observations

The Met Office Hadley Centre homogenized and quality controlled, integrated sub-daily data set (HadISDH; Willett et al., 2014, 2020) blends marine and land near-surface temperature and humidity fields over the period 1973–2020 (version 1.0 is constructed from HadISDH.land v4.2.0 and HadISDH.marine v1.0.0) which are averaged onto a 5 × 5 degree latitude-longitude grid. Data since 1979 is used in the present study and this is further merged with ERA5 near-surface data (mapped onto the HadISDH grid) by reconstructing absolute values and recalculating anomalies to produce an additional globally complete filled version. This ensures that the large areas of missing data do not accentuate the substantial coverage bias and therefore complements previous assessments rather than providing a new version of the data. Without this merging, the global mean changes are dominated by varying geographic coverage that results in spurious negative trends in moisture and temperature when no account is made for the missing regions (see Figure S6 in Supporting Information S1). The un-merged HadISDH product was also considered, as was an earlier Hadley Centre and Climate Research Unit global surface humidity data set (HadCRUH; Willett et al., 2008).

Table 1
Global Mean Specific Humidity (q), Column Integrated Water Vapor (CWV) and 2 m Temperature (T_{2m}) Over 1995–2014 for Model amip and Historical Experiments, ERA5 and Observationally Based Estimates (HadCRUT5 T_{2m}; HadISDH/ERA5 q_{2m}; SSMI(S)/ERA5 CWV; AIRS $q_{700,400}$)

Model/experiment	T_{2m} (K) hist	T_{2m} (K) amip	q_{2m} (g/kg) hist	q_{2m} (g/kg) amip	CWV (kg/m²) hist	CWV (kg/m²) amip	q_{700} (g/kg) hist	q_{700} (g/kg) amip	q_{400} (g/kg) hist	q_{400} (g/kg) amip
ACCESS-ESM1-5[a]	288.5	287.7	10.6	10.3	25.5	24.7	3.3	3.2	0.55	0.53
BCC-CSM2-MR[b]*	288.6	287.7	9.7	—	25.5	24.9	3.4	3.3	0.56	0.53
BCC-ESM1[b]*	288.5	287.7	10.0	—	27.0	26.3	3.8	3.7	0.69	0.67
CanESM5*	287.9	287.9	11.9	11.8	24.5	24.1	3.1	3.1	0.58	0.54
CESM2[d]	288.0	287.4	10.5	10.2	25.7	24.9	3.4	3.3	0.58	0.53
CESM2-WACCM[d]	287.9	287.4	10.4	10.2	25.6	24.9	3.4	3.3	0.58	0.54
CMCC-CM2-SR5[e]*	288.3	287.5	10.5	10.3	26.6	25.7	3.5	3.3	0.65	0.59
CNRM-CM6-1[f]	286.8	287.3	9.5	9.7	23.2	24.1	3.0	3.2	0.46	0.51
CNRM-ESM2-1[f]	287.5	287.4	9.8	9.7	24.0	24.0	3.2	3.2	0.49	0.51
GFDL-ESM4[g]	287.2	287.2	10.0	10.0	23.5	23.9	3.2	3.2	0.46	0.48
GISS-E2-1-G[h]*	287.6	287.5	10.5	10.2	27.2	26.0	3.8	3.6	0.64	0.60
HadGEM3-GC31-MM[i]	287.7	287.7	9.9	10.0	24.6	24.9	3.3	3.3	0.51	0.52
INM-CM5-0[j]*	287.1	287.5	9.6	10.0	24.1	25.8	3.1	3.4	0.57	0.65
IPSL-CM6A-LR[k]	287.0	287.2	9.9	10.1	24.9	25.6	3.4	3.5	0.45	0.48
MIROC6[l]	289.0	288.9	10.4	10.5	25.8	26.6	3.7	3.8	0.55	0.60
MRI-ESM2-0[m]	287.6	287.8	10.4	10.6	24.5	25.2	3.3	3.4	0.55	0.57
NorESM2-LM[n]*	288.2	287.6	10.3	10.1	26.4	25.8	3.5	3.5	0.65	0.61
UKESM1-0-LL[o]	287.2	287.7	9.8	10.0	24.2	24.7	3.2	3.3	0.52	0.53
Ensemble mean	287.8	287.6	10.2	10.2	25.2	25.1	3.4	3.4	0.56	0.55
ERA5[p]*	287.5		9.8		24.2		3.2		0.50	
Observations[p,q]	287.5		9.8		24.8		3.2		0.48	

Note. *Pressure level data below surface filled by extrapolation.
[a]Ziehn et al. (2020). [b]Wu et al. (2019). [c]Swart et al. (2019). [d]Gettelman et al. (2019). [e]Lovato et al. (2021) and Scoccimarro et al. (2021). [f]Séférian et al. (2019) and Voldoire et al. (2019). [g]Zhao et al. (2018). [h]Elsaesser et al. (2017). [i]Andrews et al. (2020). [j]Song et al. (2021). [k]Boucher et al. (2020). [l]Tatebe et al. (2019). [m]Yukimoto et al. (2019). [n]Seland et al. (2020). [o]Swaminathan et al. (2021). [p]Hersbach et al. (2020). [q]Morice et al. (2021), Willett et al. (2014, 2020), Wentz (1997), Tian and Hearty (2020).

2.3. Climate Models

An ensemble of climate model simulations contributing to the CMIP6 *historical* and *amip* experiments were selected (Table 1) based on the availability of diagnostics including near-surface and atmospheric pressure-level specific and relative humidity and temperature as well as column integrated water vapor. Although the full set of CMIP6 models is not considered, doing so would still not ensure the full range of uncertainty is captured and the set of 18 models is considered a suitable number to sufficiently represent internal variability as well as model structural uncertainty. This is a reasonable assumption given that interannual relationships between temperature and moisture are tightly constrained across a similar size CMIP6 ensemble as well as for larger CMIP5 and large single model ensembles (Santer et al., 2021).

The *historical* experiments apply realistic changes in radiative forcings to coupled versions of the climate models over the period 1850–2014 (the 1979–2014 subset is extracted). The *amip* experiments apply realistic radiative forcings, sea surface temperature (SST) and sea ice distributions to force the land surface and atmosphere-only components of the models over 1979–2014. Ensemble members r1i1p1f1 were used apart from CNRM models (r1i1p1f2), UKESM (r1i1p1f2 for historical, r1i1p1f4 for amip) and HadGEM3 (r1i1p1f3) which accounts for slight adjustments to forcings required to produce the required CMIP6 simulations. Only some models filled pressure level data below the surface by extrapolation (BCC-CSM2-MR, BCC-ESM1, CanESM5, GISS-E2-1-G, INM-CM5-0, CMCC-CM2-SR5, NorESM2-LM). It was decided not to investigate filling unsampled regions

in the remaining models due to the small sensitivity of AIRS results to filling using ERA5 (only noticeable at 925 hPa and <10% difference in global mean trend and sensitivity to interannual surface temperature changes; see Figure S2 in Supporting Information S1).

In general, the CNRM models simulate the driest atmosphere, even where observed SSTs are prescribed in the *amip* simulations; the IPSL upper troposphere is notably dry compared to other models (Table 1 and Table S1 in Supporting Information S1) though comparable with the ERA5 and the AIRS 400 hPa estimates (Table 1). The CNRM models also simulate relatively low specific humidity at 400 hPa, though this appears mainly related to a relatively cold upper troposphere rather than low relative humidity (Table S1 in Supporting Information S1). The CanESM5 model produces the highest near-surface moisture amount and relative humidity (Table 1 and Table S1 in Supporting Information S1) and the BCC-ESM1 and GISS-E2 models simulate the largest tropospheric moisture totals with most models overestimating water vapor amounts compared to ERA5 and the observations-based estimates. The MIROC model simulates unusually high global surface temperature, even in the *amip* experiment where SSTs are constrained by observations with land regions, therefore, being unusually warm (e.g., by >10 K regionally). It is not clear whether this is due to a diagnostic or physical reason though the model does exhibit a positive net heating of about 1 Wm^{-2} in the pre-industrial spin-up simulations (Tatebe et al., 2019) and also simulates above average water vapor amount in the *amip* and *historical* simulations (Table 1). The INM-CM5-0 *amip* simulations display suspect near-surface temperature over the ocean during July–December 2014 though this does not noticeably influence the results.

2.4. Methodology

Monthly mean data from the observational (filled and unfilled) estimates, reanalysis and climate models spanning 1979–2020 and depending on the data record lengths were processed using *CDO* software (version 1.9.5; http://mpimet.mpg.de/cdo). Data sets were bi-linearly interpolated onto a common 0.75×0.75 degree latitude-longitude grid. Monthly global, tropical, and zonal means were computed over the land, ocean, and all regions using a common land-sea mask derived from the reanalysis data (land is assumed if more than half of the interpolated grid points are land points). In addition, grid point deseasonalized anomalies and relative anomalies (% deviation from climatology) and corresponding global, tropical, and zonal means were computed, though analysis primarily focuses on the absolute means: these were subsequently processed to compute absolute and relative deseasonalized anomalies of the global, tropical and zonal means using a base period of 1995–2014 (2002–2014 for AIRS, the part of this record which overlaps with this baseline), commonly used to denote "present-day" conditions (e.g., Douville et al., 2021). In the case of the SMMR/ERA5 data, anomalies were computed with respect to 1979–1984 and the area mean (e.g., global) anomalies adjusted by the area mean SMMR/ERA5 (1979–1984) minus SSMI(S)/ERA5 (1995–2014) difference.

Present-day multi-annual means and linear trends of deseasonalized anomalies were computed over various time-scales and depending on data availability (a focus was 1988–2014 based on data availability). Finally, to assess the interannual coupling of large-scale humidity and temperature variability, the linear trends are removed from the time series and the sensitivity of detrended anomalies to detrended surface temperature anomalies were computed over the same time periods. This, therefore, isolates the interannual relationship between atmospheric moisture and surface temperature that is distinct from the (multi-)decadal scale trends.

3. Results

3.1. Water Vapor Changes

Changes in global mean atmospheric water vapor and surface air temperature are displayed in Figure 1 during 1979–2020 for the observationally based data sets, ERA5 reanalysis and *amip* simulations. Interannual variability is characterized by warming and moistening during El Niño events (e.g., 1987/1988, 1997/1998, 2015/2016) with cooler and drier conditions globally during La Niña events (e.g., 1988/1989, 1998–2000, 2008/2009). Large volcanic eruptions also cause cooling which is amplified by resulting drying of the troposphere, as evident following the eruption of Mt. Pinatubo in 1991 (Soden et al., 2002).
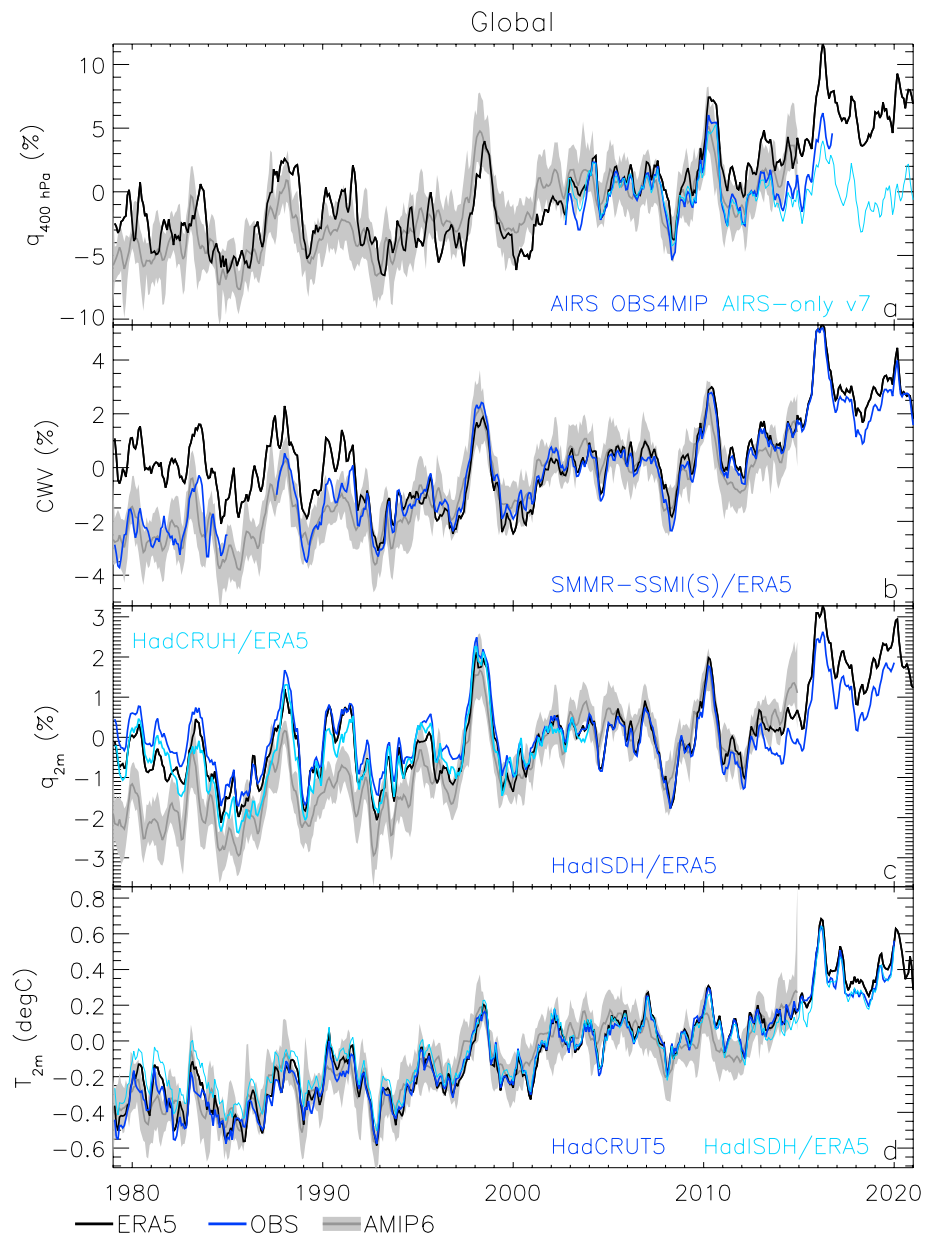
Figure 1. Deseasonalized anomaly time series of global mean atmospheric water vapor (% anomaly relative to 1995–2014 baseline) for *amip* models (ensemble mean and range) and ERA5 for (a) 400 hPa specific humidity (*q*) including AIRS satellite observations (Obs4MIP AIRS + AMSU and AIRS-only v7 products relative to 2002–2014), (b) total column integrated water vapor (CWV) including SSMI(S)/ERA5 and SMMR/ERA5 blended satellite microwave estimates and (c) near-surface specific humidity (2 m) including HadISDH/ERA5 and HadCRUH/ERA5 blended observations and (d) surface temperature (°C anomalies) including HadCRUT5 observations and the HadISDH/ERA5 blended record. A 3-month boxcar average smoothing is applied.

There is broad agreement between data sets with notable exceptions:

1. Increases in upper tropospheric specific humidity at 400 hPa (q_{400}) in simulations and ERA5 are less pronounced in AIRS observations, though interannual variability is similar (Figure 1a).
2. A decrease in ERA5 column integrated water vapor 1979–1993 conflicts with simulations and the SMMR-SSMI(S)/ERA5 blended record since 1979 with strong agreement after 1993 (anomalies within ~0.5%; Figure 1b).

3. Simulated increases in 2 m specific humidity (q_{2m}) are inconsistent with ERA5 before around 1993 and with HadISDH/ERA5 estimates over the full record (Figure 1c).

The decrease in ERA5 lower tropospheric moisture in the late 1980s/early 1990s appear consistent with a previous version of the reanalysis where they were attributed to an unrealistic influence of the changing observing system (Allan et al., 2020; Hersbach et al., 2020). This also raises questions as to the realism of the low level water vapor trends estimated by HadISDH/ERA5 (Figure 1c); since this fills missing data with ERA5, the difference to ERA5-only is indicative of the HadISDH data alone which appears to show a decrease in specific humidity relative to ERA5 over time. HadISDH/ERA5 variability is consistent with an earlier data set (HadCRUH) similarly combined with ERA5 (1979–2003), though HadCRUH/ERA5 displays near-surface specific humidity anomalies slightly closer to the *amip* simulations. The decrease in HadISDH water vapor is also apparent in differences with *amip* simulations masked to the unfilled HadISDH observations (Figure S6 in Supporting Information S1); this is dominated by the tropical oceans (not shown) and coincides with HadISDH temperature and specific humidity anomalies that are more positive than the simulations before around 1995. HadISDH/ERA5 2 m temperature anomalies are also more positive than HadCRUT5 and ERA5 in the 1980s (Figure 1d) and this is consistent with the higher 2 m specific humidity anomalies given that they are calculated using the dry bulb and dewpoint temperature (Willett et al., 2020). This highlights the challenges in constructing homogeneous climate data sets which for HadISDH involves rigorously accounting for daytime solar bias, unaspirated-psychrometer bias, ship height for ocean measurements and reporting deficiencies, all of which can change over time (Willett et al., 2020). Investigating the causes of these discrepancies merits further investigation but are beyond the scope of the present study.

3.1.1. Water Vapor Trends

Table 2 quantifies the global mean trends (dq/dt) across all data sets for 1988–2014, including the *historical* simulations which represent unforced interannual variability but are not designed to capture its correct timing. The *amip* simulations estimate a smaller magnitude increase in water vapor (around half) compared to *historical* simulations (Table 2). This is principally due to the suppressed observed warming during 1998–2013 relating partly to internal climate variability, though radiative forcing, the pattern of warming and high climate sensitivity in some CMIP6 coupled models also plays a role (Eyring et al., 2021; Forster et al., 2021; Kosaka & Xie, 2013; Mitchell et al., 2020). Corresponding 1988–2014 trends in ERA5 are increased by around 0.5%/decade throughout the troposphere when extending this period up to 2019 (Figure S2b in Supporting Information S1).

In agreement with Figure 1, simulated increases in column integrated water vapor of about 1%/decade are reproduced by the SSMI(S)/ERA5 observations-based estimate. Simulated 2 m water vapor increases are consistent with column trends but 23% smaller, while insignificant trends in HadISDH/ERA5 2 m specific humidity are at odds with the observed column integrated trends. These small trends are consistent with decreasing HadISDH minus *amip* ensemble mean water vapor anomalies computed over the observational coverage region (Figure S6 in Supporting Information S1); these are most pronounced over the tropical ocean and are also associated with a decreasing trends in HadISDH minus *amip* surface air temperature, which merits further investigation yet is beyond the scope of the present study.

Upper tropospheric (400 hPa) moisture increases by ~2%/decade in ERA5 and *amip* simulations but not in the AIRS Obs4MIP record. The discrepancy is smaller when considering the full AIRS Obs4MIP record (2003–2016) which produces ~1%/decade more positive trends (Figure S2b in Supporting Information S1), though this is influenced by the 2015/2016 El Niño warm event. Based on Figure 1 and Figure S3 in Supporting Information S1 it is not expected that the AIRS-only v7 record will alter these results substantially though there are some discrepancies early in the record and evidence of a drying trend after 2016 that is at odds with ERA5 (Figure S3 in Supporting Information S1).

Larger relative magnitude (%) moisture responses at higher altitudes (Figure S1 in Supporting Information S1) are consistent with the Clausius Clapeyron equation which determines a larger relative change in saturation vapor pressure with warming at lower temperatures (e.g., Allan, 2012) but also due to amplification of warming aloft due to diabatic and radiative processes (e.g., Ohmura, 2012). Combined with an observed global surface warming of 0.17 ± 0.01 K/decade based on HadCRUT5, the global moisture increases correspond with around 6%/K sensitivity for column integrated water vapor and a ~12%/K response of 400 hPa water vapor to surface temperature.

Table 2
Global Mean Trends (%/decade, 1988–2014) in 2 m Specific Humidity (q_{2m}), Column Integrated Water Vapor (CWV) and Specific Humidity at 400 hPa (q_{400}) for Model amip and historical Experiments, ERA5 and Observations-Based Estimates (HadISDH/ERA5 q_{2m}; SSMIS(S)/ERA5 CWV; AIRS 2002–2014 Only q_{400}) [*Significant at 90% Confidence Level Accounting for Autocorrelation; ±1 Standard Error in Linear Fit Apart From Model Ensemble ±1 Standard Deviation Model Spread.] Observations Denote HadISDH/ERA5 q_{2m}; SSMIS(S)/ERA5 CWV and AIRS (2002–2014 Only) q_{400}

Model	q_{2m}		CWV		q_{400}	
Trend (%/decade)	hist	amip	hist	amip	hist	amip
ACCESS-ESM1-5	2.09 ± 0.07*	0.81 ± 0.06*	2.55 ± 0.09*	0.92 ± 0.08*	4.33 ± 0.19*	1.69 ± 0.19*
BCC-CSM2-MR	1.37 ± 0.06*	—	1.63 ± 0.08*	0.95 ± 0.08*	2.82 ± 0.16*	1.65 ± 0.18*
BCC-ESM1	1.23 ± 0.06*	—	1.45 ± 0.08*	1.04 ± 0.08*	2.46 ± 0.16*	1.83 ± 0.18*
CanESM5	2.05 ± 0.06*	0.77 ± 0.05*	2.82 ± 0.10*	1.16 ± 0.08*	5.48 ± 0.21*	2.17 ± 0.18*
CESM2	1.52 ± 0.08*	0.86 ± 0.06*	1.89 ± 0.10*	1.13 ± 0.08*	3.52 ± 0.22*	2.30 ± 0.19*
CESM2-WACCM	1.55 ± 0.06*	0.91 ± 0.06*	1.90 ± 0.08*	1.08 ± 0.08*	3.41 ± 0.17*	2.16 ± 0.19*
CMCC-CM2-SR5	2.01 ± 0.09*	1.04 ± 0.06*	2.39 ± 0.11*	1.28 ± 0.08*	4.21 ± 0.24*	2.41 ± 0.18*
CNRM-CM6-1	1.01 ± 0.06*	0.77 ± 0.06*	1.21 ± 0.09*	0.98 ± 0.09*	2.34 ± 0.20*	2.02 ± 0.20*
CNRM-ESM2-1	1.42 ± 0.05*	0.77 ± 0.06*	1.70 ± 0.07*	0.98 ± 0.09*	3.13 ± 0.16*	1.89 ± 0.20*
GFDL-ESM4	1.53 ± 0.08*	0.85 ± 0.06*	1.94 ± 0.11*	1.19 ± 0.08*	3.82 ± 0.22*	2.25 ± 0.20*
GISS-E2-1-G	1.40 ± 0.10*	0.83 ± 0.06*	1.79 ± 0.15	0.97 ± 0.08*	3.15 ± 0.29*	1.72 ± 0.17*
HadGEM3-GC31-MM	1.92 ± 0.07*	0.81 ± 0.07*	2.23 ± 0.08*	0.92 ± 0.09*	3.75 ± 0.16*	1.67 ± 0.17*
INM-CM5-0	1.04 ± 0.06*	0.82 ± 0.06*	1.20 ± 0.07*	1.07 ± 0.07*	2.30 ± 0.13*	2.07 ± 0.15*
IPSL-CM6A-LR	1.27 ± 0.09*	0.88 ± 0.06*	1.63 ± 0.13*	1.12 ± 0.08*	3.13 ± 0.26*	2.25 ± 0.18*
MIROC6	1.58 ± 0.09*	0.74 ± 0.06*	2.09 ± 0.14*	0.96 ± 0.09*	3.75 ± 0.29*	1.93 ± 0.18*
MRI-ESM2-0	1.23 ± 0.07*	0.78 ± 0.06*	1.53 ± 0.10*	1.06 ± 0.08*	2.47 ± 0.18*	1.81 ± 0.15*
NorESM2-LM	1.73 ± 0.08*	0.92 ± 0.06*	2.11 ± 0.11*	1.14 ± 0.08*	3.67 ± 0.22*	2.08 ± 0.18*
UKESM1-0-LL	2.21 ± 0.06*	0.82 ± 0.06*	2.49 ± 0.08*	0.93 ± 0.09*	4.06 ± 0.16*	1.63 ± 0.17*
Ensemble median	1.53 ± 0.36*	0.82 ± 0.07*	1.90 ± 0.46*	1.06 ± 0.11*	3.52 ± 0.82*	2.02 ± 0.25*
ERA5	0.28 ± 0.05		0.78 ± 0.08*		2.26 ± 1.17*	
Observations	−0.04 ± 0.05		1.02 ± 0.07*		0.69 ± 0.51	

The relatively low moisture content CNRM models also produce one of the smallest %/decade near-surface water vapor trends of the *amip* simulations. Conversely, the CanESM model simulates a relatively moist near-surface but a smaller than *amip* average %/decade trend and the IPSL model simulates a dry upper troposphere yet produces one of the largest %/decade 400 hPa moisture trends. This suggests there is not a simple link between mean moisture biases and trends.

Moisture trends on pressure levels are dominated by lower latitude ocean changes where the moisture amount is larger and so global mean changes are similar to tropical ocean mean changes: tropical ocean $dCWV/dt$ is 1.77 ± 0.45%/decade in *historical* simulations (7% less than global mean trends) and 0.86 ± 0.10%/decade in *amip* (20% smaller than the global mean trend; see Figure S1 in Supporting Information S1). The smaller tropical ocean trends in *amip* simulations may reflect the larger influence of El Niño on tropical ocean variability. However, there is an 8% larger tropical ocean trend compared to the global mean for ERA5, which could partly be explained by regionally dependent inhomogeneities in observations-based data sets, that are beyond the scope of the present analysis. There is a smaller trend in ERA5 water vapor over tropical land than the global mean and compared with the *amip* simulations at all levels considered (Figure S1 in Supporting Information S1), with a non-significant *CWV* trend of 0.3%/decade compared with 0.8–1.7%/decade range for *amip* simulations. The decreasing global *CWV* trends in ERA5 before 1993 are particularly apparent for the 850 hPa level and over the tropical oceans (Figure S2 in Supporting Information S1).

While AIRS observations reproduce the interannual variability in moisture throughout the troposphere displayed by ERA5 and *amip* simulations (Figure 1a; Figure S2 in Supporting Information S1), trends are generally not

significant in the mid/upper troposphere but strongly positive in the lower troposphere (e.g., 2.6%/decade for global mean 850 hPa trends 2002–2016) and there is inhomogeneity apparent in the 925 hPa AIRS time series during early 2014 (Figure S2 in Supporting Information S1).

Computing the global mean of % water vapor anomalies is of greater relevance to the global longwave radiative effect and water vapor feedback and increases the importance of higher latitude regions: this increases low altitude global trends by ∼0.2%/decade and decreases upper tropospheric water vapor trends by up to ∼1%/decade (see ERA5 in Figure S2d in Supporting Information S1), only marginally different to the % anomalies of the global mean in Table 2.

3.1.2. Zonal Mean Moisture Variability and Trends

The dependence of moisture variability and trends as a function of latitude are presented in Figure 2. Zonal mean water vapor is computed and deseasonalized anomalies are calculated as a percentage of monthly climatological mean; a zonal mean of the grid point deseasonalized percentage anomalies are very similar (not shown). Linear trends are computed for each latitude-mean over the full available data records.

Variability in upper tropospheric water vapor (q_{300}) is smoother in the *amip* ensemble mean compared to ERA5 (as expected due to ensemble averaging) but with consistent increases in equatorial latitudes during the strong El Niño events of 1983, 1998, and also 2010. However, while the latitude-mean trends are positive (0–5%/decade) across all ensemble members and the *historical* ensemble mean (Figure 2a, right panel), ERA5 displays negative trends around Antarctic latitudes and stronger than simulated trends in the northern tropics.

Column integrated water vapor (Figures 2c–2e) displays some similar features to the upper troposphere such as the tropical El Niño signals but the latitude structure in trends differs. The largest *CWV* trends as a percentage of climatology are over Arctic latitudes: ∼2–5%/decade in *amip* simulations with ERA5 at the upper end of this range. Arctic changes agree with previous estimates based on earlier reanalyses and radiosonde data (Rinke et al., 2019), with relative trends smallest in February–March and largest in October–January. This is consistent with an increased local moisture source due to delayed freezing of the open ocean (Nusbaumer et al., 2019), though increased moisture transport also plays a role (Dufour et al., 2016; Nygård et al., 2020). Trends in *CWV* are smaller than for q_{300} in the Southern Hemisphere (0°–60°S) with the SSMI(S)/ERA5 estimates close to *amip* simulations and more positive than ERA5-only estimates, which in part relates to the apparently spurious decreases in ERA5 moisture before 1993. Although the SSMI(S)/ERA5 *CWV* record is identical to ERA5 over latitudes with no ice free ocean, such as Antarctica, differences in trends reflect the contrasting data record lengths considered. Trends over the Arctic are generally smaller in the upper troposphere (Figures 2a and 2b) than at lower levels (Figures 2c–2h), reflecting that much of the Arctic warming (and therefore moistening) is concentrated in the lower troposphere(e.g., Steiner et al., 2020).

Near-surface water vapor changes (Figures 2f–2h) broadly match those for *CWV* but with less prominent tropical El Niño signals. The unfilled HadISDH latitudinal variability and trends (Figure 2h) show similarity to ERA5 but with negative trends apparent in the Southern Hemisphere, particularly before 2015. Dunn et al. (2017) identified weaker global water vapor increases since 1973 in HadISDH compared with coupled models from the CMIP6 predecessor (CMIP5); this was particularly so for the 1996–2015 period which can partly be explained by the stronger warming in CMIP5 *historical* experiments than observations over the period, consistent with CMIP6 (Mitchell et al., 2020).

Larger trends in *historical* experiments compared to *amip* (Figures 2a, 2c and 2f right panels) are particularly prominent in the northern tropics but also in the Southern Hemisphere extra-tropics for *CWV* and q_{2m}. Weak trends in HadISDH q_{2m} over the Southern Hemisphere were reported by Dunn et al. (2017); negative trends over southern mid-latitudes appear to reverse after 2014 (Figure 2). While Dunn et al. (2017) noted the model underestimate in 2 m relative humidity decline over land, the discrepancy in water vapor trends is particularly acute over the tropical ocean (Figures S1–S2 in Supporting Information S1): HadISDH/ERA5 shows a non-significant negative trend of −0.3%/decade compared to significant increases in *amip* (0.5–0.8%/decade) and *historical* simulations (0.8–2.1%/decade).

3.1.3. Sensitivity of Water Vapor Changes to Surface Temperature

Construction of decadal-scale data sets of climate-quality is limited by issues of homogeneity, sampling, and record length (Hersbach et al., 2020; Schröder et al., 2018; Simmons et al., 2014; Willett et al., 2020). Interannual
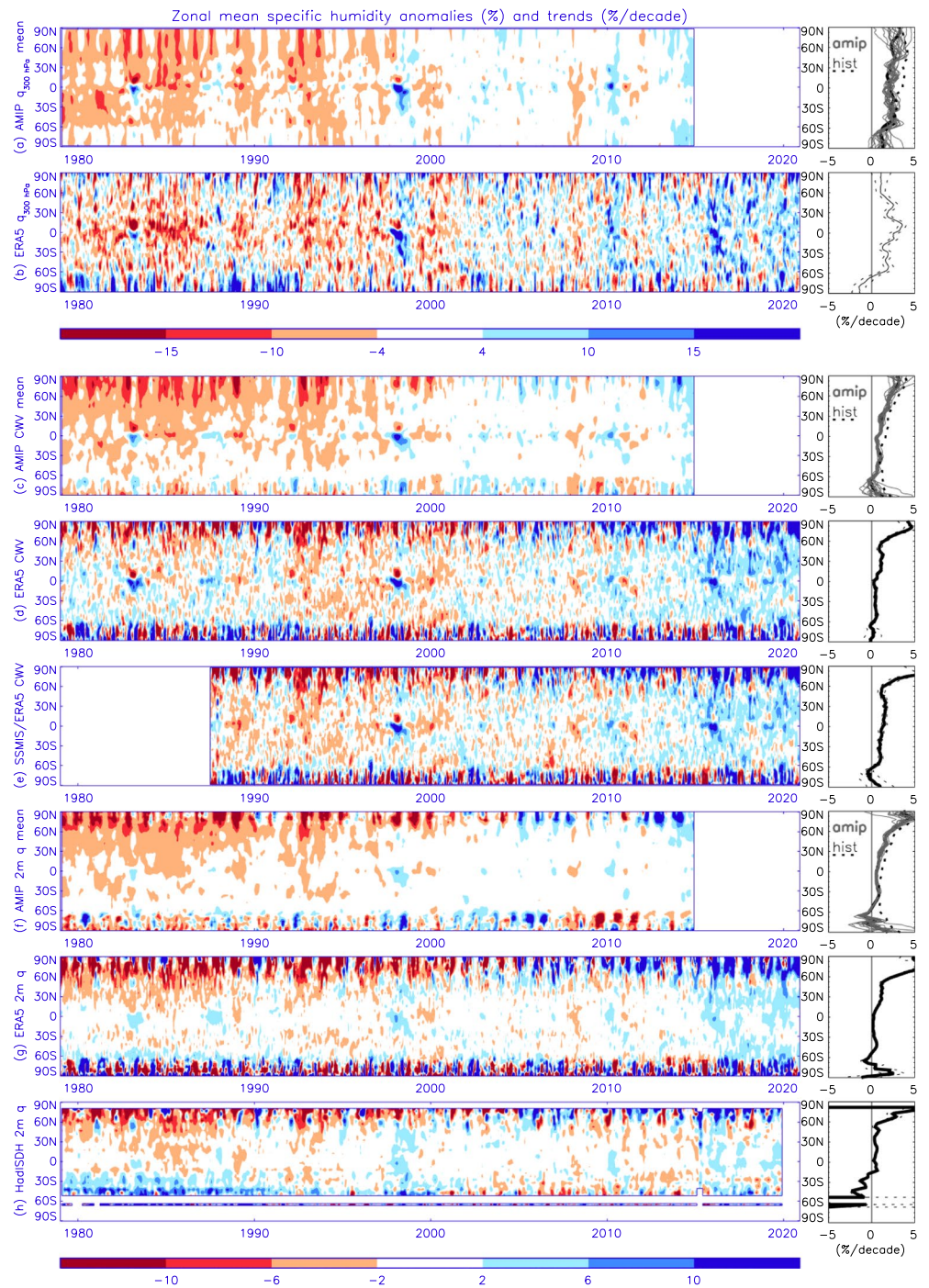
Figure 2. Time-latitude variability and trends for: 300 hPa specific humidity (a) model ensemble mean amip simulations and 1979–2014 trends for each model (gray) and ensemble mean historical experiment trend (dashed thick), (b) ERA5 (1979–2020); column integrated water vapor for (c) model ensemble mean amip simulations (trends as in (a)), (d) ERA5 (1979–2020), (e) SSMI(S)/ERA5 (1987–2020); 2 m specific humidity in (f) model ensemble mean amip simulations (trends as in (a)), (g) ERA5, (h) HadISDH (1979–2019). The time-latitude plots (left) depict % anomalies relative to zonal monthly mean (1995–2014) while zonal mean trends (right) apply for the respective record lengths with ±2 standard error on the calculated trends in ERA5 and observations (dashed).

Table 3
Global Mean Sensitivity of Detrended Water Vapor to Surface Temperature (%/K) Over 1988–2014 for amip and historical Simulations, ERA5 and Observation-Based Estimates for 2 m Specific Humidity (q_{2m}), Column Integrated Water Vapor (CWV) and Specific Humidity at 400 hPa (q_{400}) [*Significant at 90% Confidence Level Accounting for Autocorrelation; ±1 Standard Error in Linear Fit Apart From Model Ensemble ±1 Standard Deviation Model Spread.] Observations Denote HadISDH/ERA5 q_{2m}; SSMIS(S)/ERA5 CWV and AIRS (2002–2014 Only) q_{400}

Model	q_{2m}		CWV		q_{400}	
Sensitivity (%/K)	*hist*	*amip*	*hist*	*amip*	*hist*	*amip*
ACCESS-ESM1-5	4.08 ± 0.21*	4.20 ± 0.21*	5.02 ± 0.31*	5.23 ± 0.31*	8.35 ± 0.74*	10.13 ± 0.82*
BCC-CSM2-MR	3.91 ± 0.20*	—	4.59 ± 0.31*	4.37 ± 0.30*	8.49 ± 0.63*	8.13 ± 0.68*
BCC-ESM1	3.60 ± 0.24*	—	4.81 ± 0.33*	4.78 ± 0.29*	8.91 ± 0.70*	9.46 ± 0.67*
CanESM5	3.86 ± 0.19*	3.48 ± 0.19*	5.60 ± 0.31*	4.61 ± 0.33*	10.98 ± 0.74*	8.15 ± 0.77*
CESM2	5.32 ± 0.18*	4.15 ± 0.21*	6.14 ± 0.28*	5.44 ± 0.31*	11.88 ± 0.77*	10.65 ± 0.77*
CESM2-WACCM	4.42 ± 0.20*	3.86 ± 0.21*	5.04 ± 0.30*	4.80 ± 0.31*	9.04 ± 0.69*	9.74 ± 0.75*
CMCC-CM2-SR5	4.99 ± 0.16*	3.79 ± 0.22*	6.37 ± 0.23*	4.76 ± 0.32*	12.00 ± 0.55*	9.45 ± 0.73*
CNRM-CM6-1	4.70 ± 0.23*	4.17 ± 0.24*	6.25 ± 0.33*	5.08 ± 0.34*	13.50 ± 0.82*	11.40 ± 0.78*
CNRM-ESM2-1	3.91 ± 0.23*	4.25 ± 0.23*	4.83 ± 0.33*	5.43 ± 0.32*	9.41 ± 0.73*	11.84 ± 0.78*
GFDL-ESM4	5.50 ± 0.17*	4.05 ± 0.22*	7.10 ± 0.27*	5.05 ± 0.35*	12.64 ± 0.62*	10.75 ± 0.88*
GISS-E2-1-G	6.01 ± 0.23*	4.00 ± 0.26*	8.67 ± 0.35*	4.84 ± 0.39*	16.76 ± 0.74*	8.88 ± 0.84*
HadGEM3-GC31-MM	4.72 ± 0.18*	4.43 ± 0.23*	5.59 ± 0.24*	5.08 ± 0.33*	9.06 ± 0.53*	9.31 ± 0.69*
INM-CM5-0	4.40 ± 0.18*	3.55 ± 0.18*	4.96 ± 0.25*	3.99 ± 0.26*	8.46 ± 0.51*	7.11 ± 0.62*
IPSL-CM6A-LR	4.95 ± 0.16*	3.74 ± 0.20*	6.67 ± 0.25*	4.56 ± 0.32*	12.62 ± 0.60*	8.28 ± 0.75*
MIROC6	6.20 ± 0.19*	3.72 ± 0.22*	9.36 ± 0.31*	4.90 ± 0.32*	18.29 ± 0.68*	8.75 ± 0.70*
MRI-ESM2-0	4.18 ± 0.27*	3.23 ± 0.20*	5.45 ± 0.40*	3.83 ± 0.28*	8.83 ± 0.76*	6.19 ± 0.58*
NorESM2-LM	5.54 ± 0.18*	3.83 ± 0.21*	7.02 ± 0.26*	4.77 ± 0.30*	12.42 ± 0.61*	9.35 ± 0.70*
UKESM1-0-LL	4.08 ± 0.22*	4.53 ± 0.23*	4.55 ± 0.30*	5.43 ± 0.34*	7.31 ± 0.70*	9.69 ± 0.71*
Ensemble median	4.70 ± 0.77*	4.00 ± 0.35*	5.60 ± 1.37*	4.84 ± 0.45*	10.98 ± 3.01*	9.45 ± 1.42*
ERA5	4.45 ± 0.22*		5.76 ± 0.35*		10.20 ± 0.84*	
Observations	4.41 ± 0.24*		5.53 ± 0.36*		9.89 ± 1.51*	

variability is, however, more robustly represented (Figure 1 and Figures S2–S3 in Supporting Information S1). Such variability in water vapor or precipitation are often utilized to test the coupling with surface temperature on these time-scales and infer links to climate change (Adler et al., 2008; Allan & Soden, 2008; Dessler et al., 2008) with the caveat that there is not a simple link between interannual and multi-decadal responses.

Interannual coupling is now assessed in models, reanalyses and observation over the period 1988–2014 through linear regression of detrended water vapor (surface to 300 hPa pressure level % anomalies) and surface temperature anomalies (see Section 2.4) for the global and tropical mean and corresponding ocean-only and land-only estimates (Table 3; Figure 3). The interannual sensitivity of detrended moisture to surface temperature anomalies (dq/dT_s) therefore provides distinct yet complimentary information relative to the corresponding sensitivity computed from multi-decadal trends in moisture and surface temperature ((dq/dt)/(dT_s/dt)).

At higher levels in the troposphere, global mean moisture responds more strongly to surface temperature changes (~4–5%/K near the surface and up to ~10%/K at 400 hPa) in *amip* simulations, reanalyses, and observations (Table 3, Figure 3a). This is expected from the temperature dependence of the Clausius Clapeyron equation and the lower temperatures at higher altitudes (e.g., Allan, 2012). Dessler et al. (2008) presented a qualitatively similar picture considering global and tropical mean changes between 2007 (warm event) and 2008 (cold event). Responses are below the saturation vapor pressure rate (~6–7%/K near the surface up to about 15%/K in the upper troposphere) though this depends on the regional pattern in temperature changes and the larger moisture amounts in lower latitudes. Responses in temperature lapse rate also contribute, explaining the stronger increases with altitude over the oceans (Figure 3b) and in the tropics (Figures 3d and 3e) where the atmospheric thermal structure is
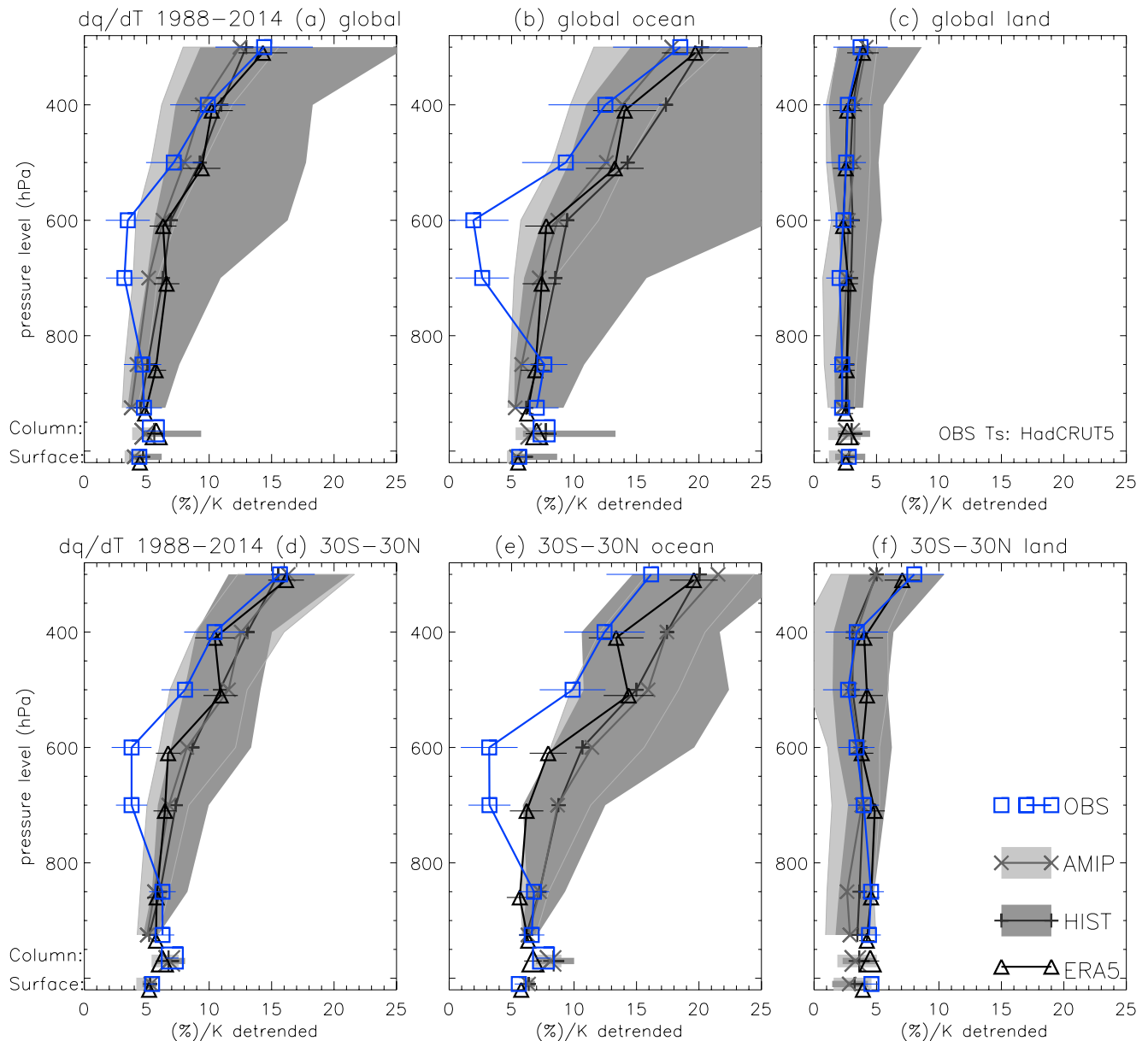
Figure 3. Detrended linear regression between atmospheric water vapor and HadCRUT5 surface temperature (%/K) for the (a) global land and ocean, (b) global ocean, (c) global land, (d) tropical land and ocean, (e) tropical ocean and (f) tropical land over 1988–2014 for *amip* and *historical* model experiments (line denotes ensemble median and shading the range), ERA5, AIRS satellite observations (2002–2014), SSMI(S)/ERA5 column integrated water vapor and HadISDH/ERA5 2 m observations (horizontal lines denote 90% uncertainty ranges).

more strongly constrained by the moist adiabatic lapse rate. Over land (Figure 3c), there are weaker sensitivities (~2–5%/K) with little altitude dependence apart from in the tropics at altitudes higher than the 400 hPa level (Figure 3f). The weaker sensitivities are in part explained by the larger land surface temperature anomaly relative to the ocean surface temperature anomaly (not shown).

Regional variations in moisture sensitivity are partly explained by a greater upper tropospheric temperature response than the surface over ocean (Figure 4b), particularly the tropical oceans (Figure 3e). The weaker atmospheric moisture response to temperature variation over land is partly explained by a steepening of temperature lapse rates during warmer years as implied by the smaller upper tropospheric temperature response to surface warming over land (Figure 4c). These regional differences are dominated by El Niño variability which exhibits a particular pattern of ocean warming and corresponding lapse rate responses that contrast with long term trends
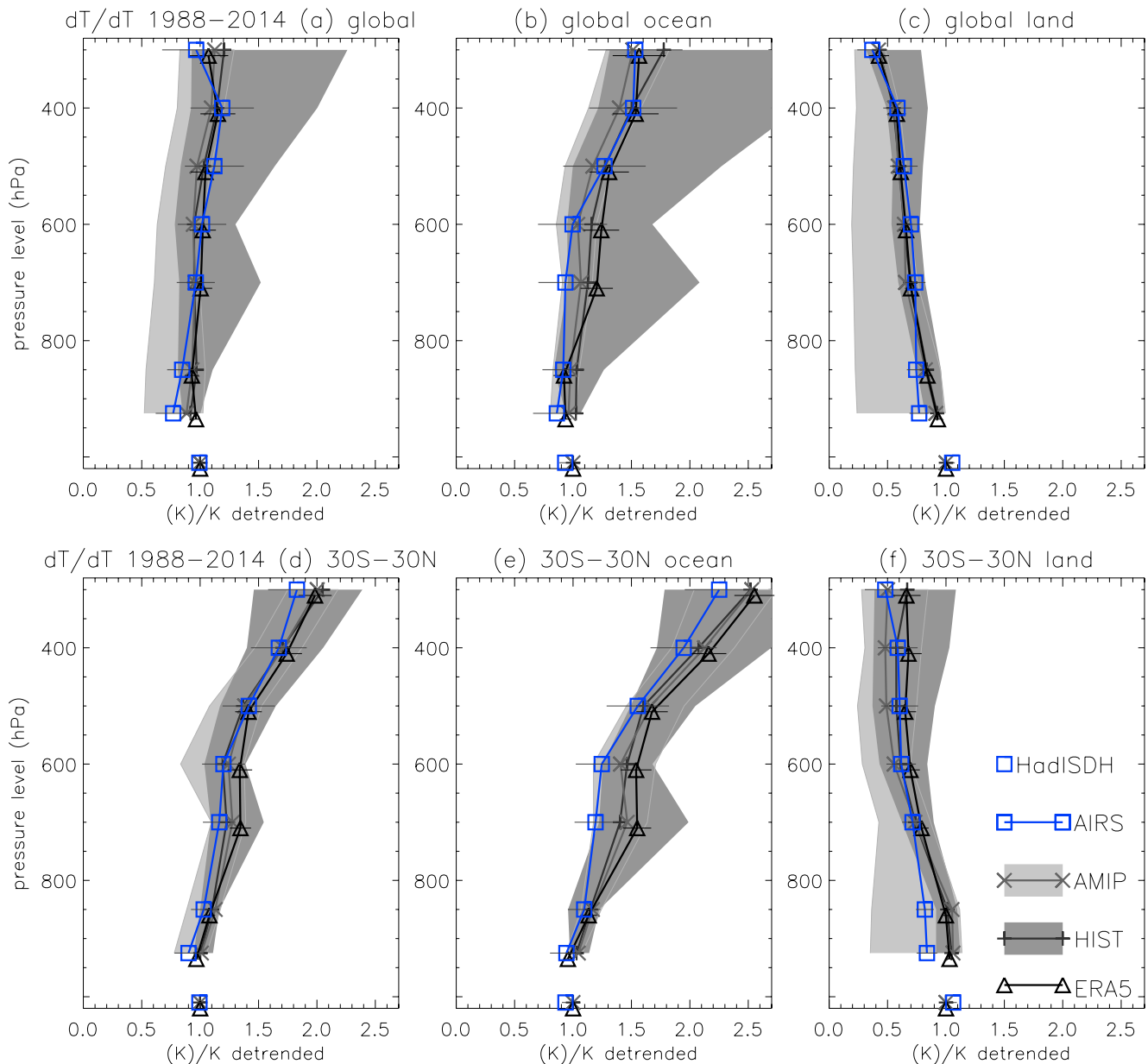
Figure 4. Detrended linear regression between in atmospheric temperature and HadCRUT5 surface temperature (%/K) for the (a) global land and ocean, (b) global ocean, (c) global land, (d) tropical land and ocean, (e) tropical ocean and (f) tropical land over 1988–2014 for *amip* and *historical* model experiments (ensemble median±1 standard deviation), ERA5, AIRS satellite observations (2002–2014) and HadISDH 2 m observations.

(1988–2014). Multi-decadal temperature trends appear more consistent between ocean and land though with less similarity between data sets (Figure S4 in Supporting Information S1). Tropospheric temperature trends in ERA5 are up to about 0.1 K/decade weaker than simulated by the *amip* ensemble mean (Figure S4 and Table S2 in Supporting Information S1), which itself shows suppressed warming compared to the coupled *historical* experiment (by 0.1–0.2 K/decade). The smaller warming in *amip* than *historical* simulations is again partly explained by internal variability (Kosaka & Xie, 2013; Mitchell et al., 2020), but the long-term evolving pattern of warming and the realism of climate sensitivity may also play a role.

There is greater consistency in interannual moisture and temperature responses across data sets compared with multi-decadal trends. AIRS Obs4MIP displays a smaller mid and upper tropospheric water vapor sensitivity to surface temperature than other data sets, particularly around 600–700 hPa over the tropical oceans where
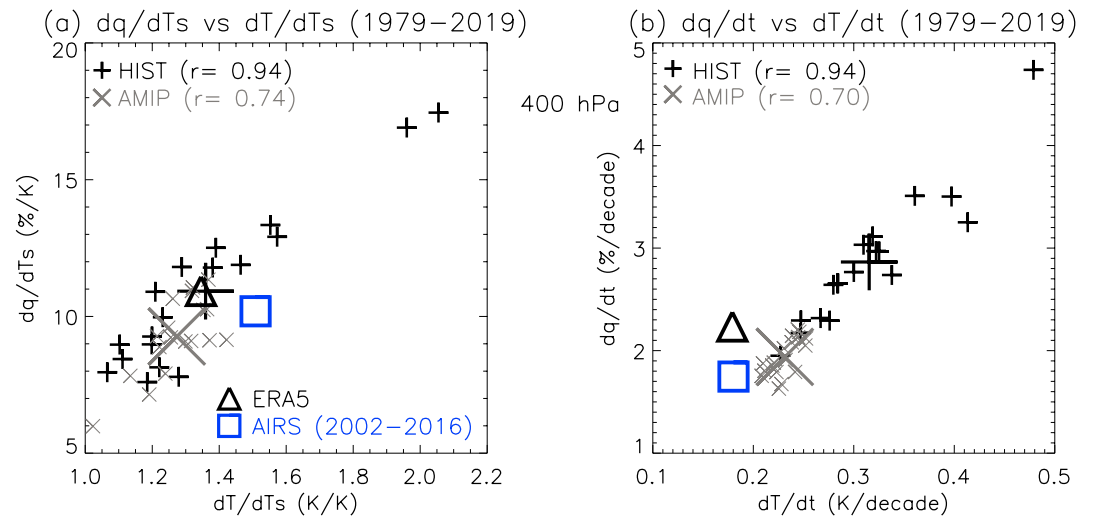
Figure 5. Responses of global mean upper tropospheric water vapor and temperature responses across models (*amip* and *historical* experiments 1979–2014; large symbol denotes ensemble mean) and for ERA5 (1979–2019) and AIRS observations (2002–2016): (a) detrended linear regression between 400 hPa water vapor and surface temperature (*dq/dTs*) scattered against 400 hPa temperature regression with surface temperature (*dT/dTs*); (b) 400 hPa water vapor trends scattered against 400 hPa temperature trends.

mid-tropospheric temperature responses are also smaller than other data sets. This is for a shorter period than other data sets (2002–2014 in Figures 3 and 4) and extending to 2016 increases the sensitivity by around 1%/K throughout most of the troposphere (Figure S2a in Supporting Information S1). Applying the AIRS-only v7 record up to present is however not anticipated to alter this discrepancy based on Figure 1a and Figure S3 in Supporting Information S1 comparisons. The interannual sensitivity is also relatively robust to time period, detrending, and sampling compared with trends (see Supplementary Information; Figure S2 in Supporting Information S1).

Despite discrepancies between long term trends in q_{2m} and *CWV* between HadISDH-ERA5 and *amip* simulations, interannual responses are consistent and within the model ranges. The MRI-ESM2 *amip* simulation produce the smallest interannual sensitivity at all levels while the CNRM models simulate the largest upper tropospheric water vapor sensitivity to surface temperature variability (>11%/K; Table 3) despite 1988-2014 trends that are close to the ensemble median (Table 2). This is explained by the atmospheric temperature response to interannual surface temperature changes which is small in MRI-ESM2 and large in the CNRM models (Table S3 in Supporting Information S1). However, the substantial range in (detrended) upper tropospheric interannual *dq/dT* sensitivities exhibited by the *historical* experiments (7.3–18.3%/K; Table 3) indicates a diversity in unforced climate variability generated by the coupled climate models in terms of magnitude and spatial or temporal characteristics.

3.1.4. Links Between Tropospheric Temperature and Moisture Variability

Thermodynamic coupling between temperature and water vapor is confirmed by considering the interannual and multi-decadal relationships across data sets, illustrated for the 400 hPa level in Figure 5 for full data records within the 1979–2019 period. There is a robust relationship between water vapor and temperature responses over interannual (Figure 5a) and multi-decadal (Figure 5b) scales across models that are in broad agreement with ERA5 and AIRS values. ERA5 produces a large water vapor trend relative to its 400 hPa temperature trend (Figure 5b) in comparison with AIRS and the models. However, temperature and moisture trends in AIRS and ERA5 are smaller than the *amip* simulations for the shorter 1988–2014 period (2002–2014 for AIRS; Figures S1 and S4 in Supporting Information S1).

The range of *historical* experiment multi-decadal water vapor trends is partly explained by the range of warming rates (Figure 5b) with a strong relationship across models between 400 hPa temperature and moisture trends ($r = 0.94$). For example, the CanESM5 model simulates a 400 hPa warming of 0.48 K/decade and moistening of 4.8%/decade while the MRI-CM2 model simulates a weak warming and moistening of 0.23 K/decade and 2.0%/decade (corresponding temperature trends for 1988–2014 in Table S2 in Supporting Information S1). A relationship between temperature and moisture trends also exists across *amip* simulations, albeit weaker ($r = 0.7$).

A weaker relationship is expected since the range in surface warming is constrained by the experimental design (0.14–0.17 K/decade; Table S2 in Supporting Information S1) so trends are smaller compared to internal variability. However, the magnitude and range in 400 hPa temperature trends is larger (0.21–0.25 K/decade; Figure 5b), indicating amplified upper tropospheric signal and a diversity in coupling between the upper troposphere and surface temperature. This is confirmed by considering the interannual sensitivity of upper tropospheric temperature and moisture to surface temperature (Figure 5a) which shows a significant positive relationship across models with albeit weaker correlation in *amip* ($r = 0.74$) compared to *historical* ($r = 0.94$).

Models with a stronger interannual upper troposphere temperature response to surface warming therefore also display a stronger upper tropospheric water vapor response: the MIROC6 *historical* simulation produces a strong global mean 400 hPa water vapor and temperature response to surface temperature (17.5%/K and 1.8 K/K for 1979–2014) while the MRI model displays a weak coupling (8%/K and 1.1 K/K; corresponding 1988–2014 responses in Table 3 and Table S3 in Supporting Information S1). Combining these estimates suggests a more consistent coupling between 400 hPa moisture and temperature of 9.7%/K for MIROC6 and 7.3%/K for MRI-ESM2, approximately 1%/K larger than (so quite close to) their respective *amip* experiment interannual sensitivities.

A greater amplification of upper tropospheric warming can be partly explained by a larger tropical to global warming ratio. This is suggested based on a weak positive correlation between 400 hPa temperature trends and the ratio of tropical to global surface warming trend across *historical* simulations (Figure S5 in Supporting Information S1). This can further partly explain a positive relationship between 400 *hPa* specific humidity trends and the tropical to global warming ratio ($r = 0.49$). Proportionally greater warming in the convective tropics, which is more strongly constrained by the moist adiabatic lapse rate than at higher latitudes or in subsidence regions, therefore favors a greater upper tropospheric warming and, through thermodynamic constraints, larger water vapor responses to warming. However, a diversity in patterns of warming in *historical* experiments across models (the "pattern effect", e.g., Stevens et al., 2016) does not apply to the *amip* simulations since the evolving pattern of ocean warming is constrained to be near-identical across model simulations. Therefore additional factors such as contrasting convection schemes and additional parametrizations must also contribute (e.g., Allan et al., 2002). Notably, the MRI-ESM2 model simulates one of the weakest upper tropospheric amplification of surface warming in both *historical* and *amip* experiments and across time-scales (interannual and multi-decadal).

Since greater amplification of warming aloft leads to greater outgoing longwave radiative emission, while the associated larger moisture increases reduces this longwave emission, there is a well understood strong compensation between the negative temperature lapse rate feedback and the positive water vapor feedback (Allan et al., 2002; Colman & Soden, 2021). Therefore it is useful to consider the range in combined lapse rate and water vapor feedbacks as well as a relative humidity feedback in assessing the contribution to uncertainty in climate sensitivity (Forster et al., 2021). The combined temperature and water vapor feedback is the total clear-sky radiative feedback relating to temperature and water vapor changes, often simplified as a constant relative humidity feedback given the tropospheric temperature changes. The relative humidity feedback relates to deviations away from constant relative humidity alone. The next section assesses changes in relative humidity across data sets, considering tropical ocean and land and near-global trends across lines of latitude.

3.2. Tropospheric Relative Humidity Changes

As expected from the strong thermodynamic constraint on atmospheric moisture, changes in relative humidity are small when averaging over large areas and limiting the effect of changes in atmospheric circulation changes: generally monthly anomalies in near-global relative humidity are within ±1% RH based on ERA5 and microwave and infrared UTH measurements since 1979 (John et al., 2021).

Considering first the tropics (30°S–30°N), variability is similar in magnitude over the tropical ocean and land (Figures 6a–7a) for UTH observations though is larger for ERA5 400 hPa RH (~±2%). This is partly explained by UTH being a weighted average of RH over a broad atmospheric layer (~200–500 hPa in the tropics), though AIRS estimates of tropical mean 400 hPa relative humidity are strongly correlated with both UTH estimates (MW $r = 0.85$; HIRS $r = 0.79$) and ERA5 ($r = 0.83$) over the 2003–2015 period. While previous studies have more consistently compared models and observations by simulating satellite humidity channel brightness temperatures
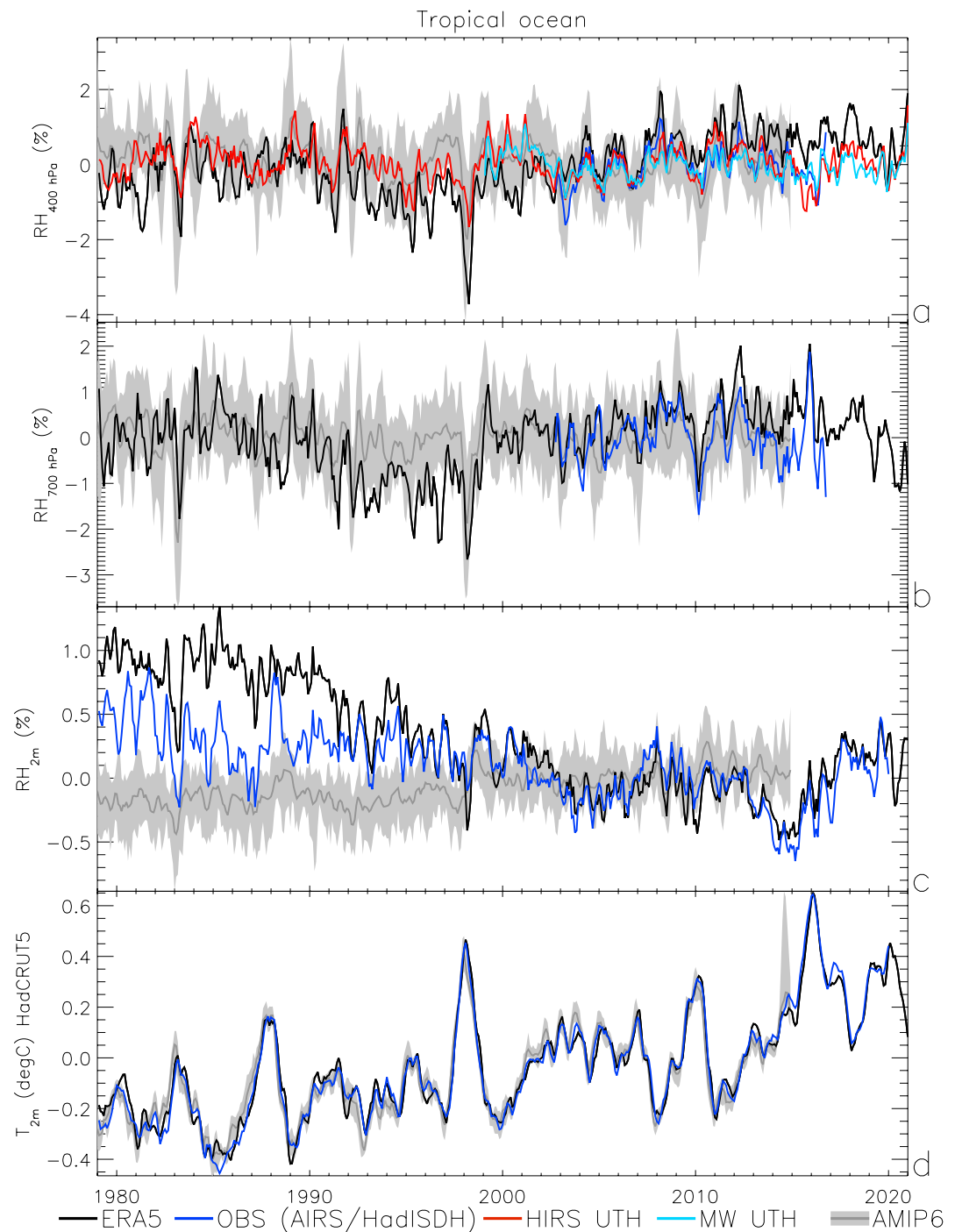
Figure 6. Deseasonalized anomaly time series of relative humidity (RH) for *amip* models (ensemble mean and range) and ERA5 at (a) 400 hPa including AIRS satellite observations and upper tropospheric humidity estimates from infra-red (HIRS) and microwave (MW) satellite observations, (b) 700 hPa including AIRS and (c) at the surface (2 m) including HadISDH observations and (d) surface temperature including HadCRUT5 observations.

(Allan et al., 2003; Soden et al., 2005), this is beyond the scope of the present work which is deemed adequate for the purposes of a qualitative comparison.

There is good qualitative agreement in interannual RH variability over the tropical ocean across data sets (Figure 6a) with decreased humidity during mature El Niño events, particularly in northern hemisphere spring
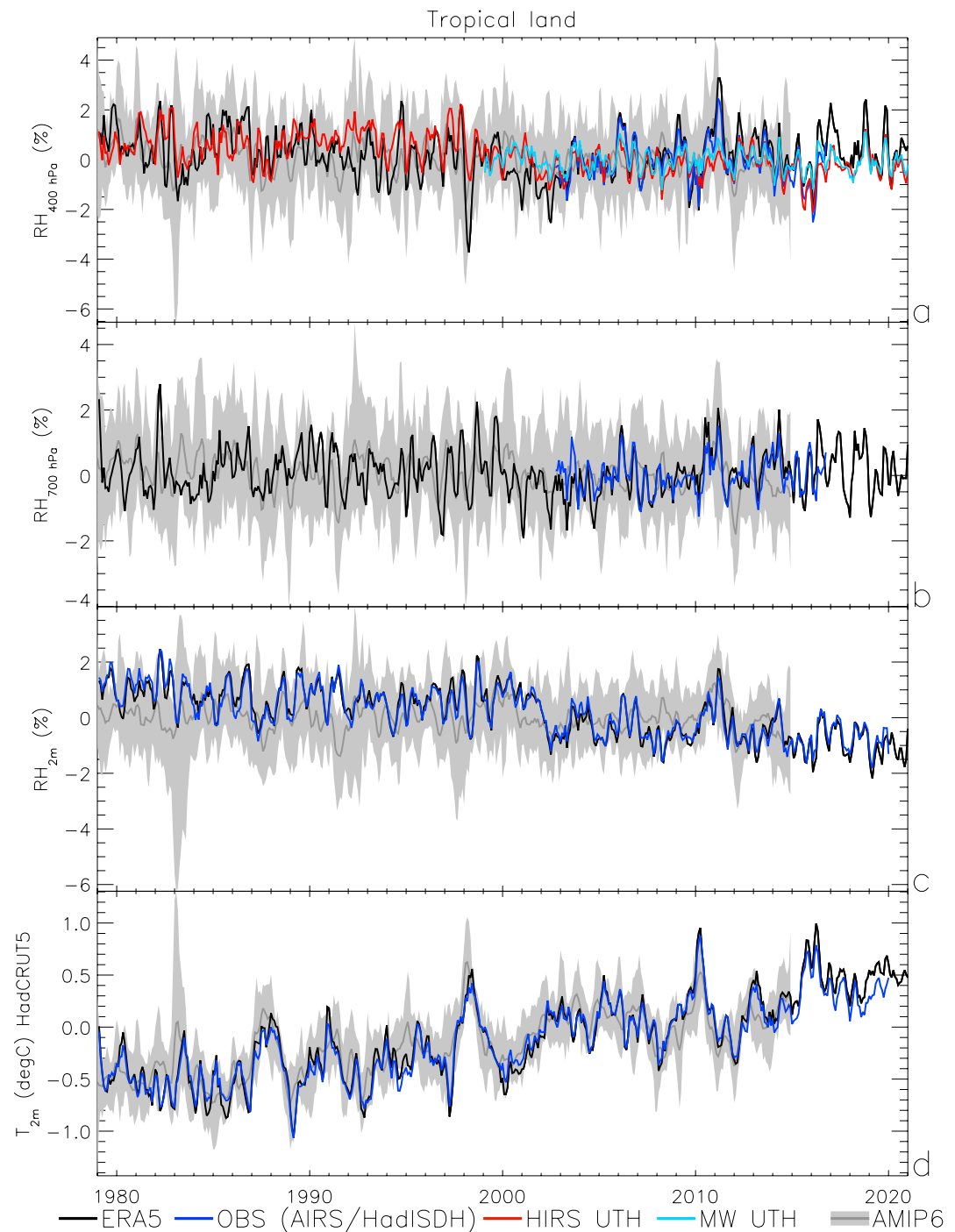
Figure 7. As Figure 6 but for tropical land.

(e.g., April in 1983, 1998, 2016) and relating partly to exceptionally strong subtropical subsidence in the Pacific (e.g., McCarthy & Toumi, 2004). Discrepancies include larger multi-decadal RH variability in ERA5 with negative anomalies generally before 2002 and positive anomalies after, in contrast to the *amip* simulations and HIRS infrared UTH estimates which tend to display negative trends. Anomalies are up to 1% RH more negative in ERA5 than the *amip* ensemble mean during 1993–1997 and this is also apparent at the 700 hPa level (Figure 6b).
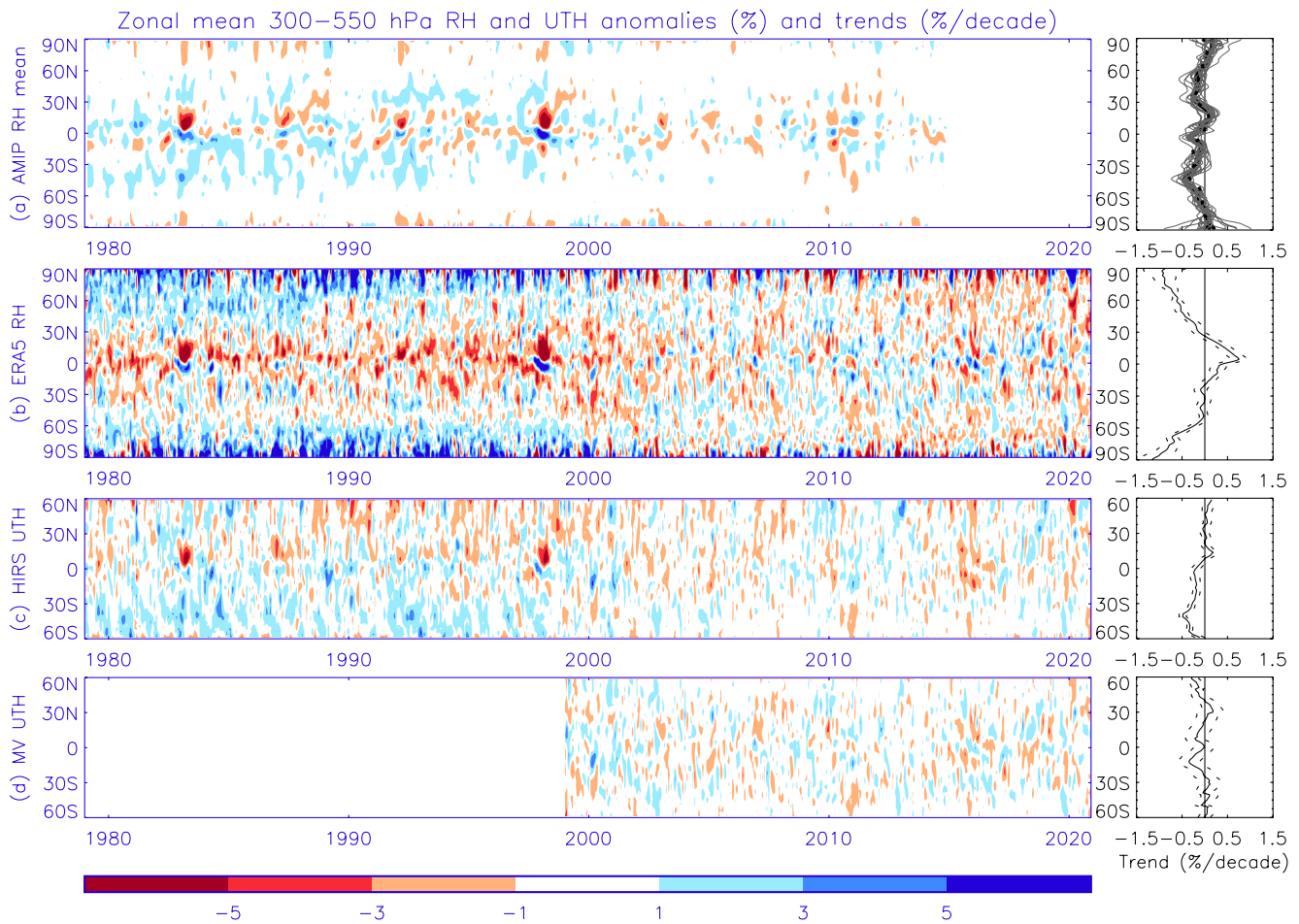
Figure 8. Time-latitude relative humidity variability and trends for (a) 300–500 hPa RH model ensemble mean *amip* simulations and 1979–2014 trends for each model (gray) and ensemble mean historical experiment trend (dashed thick); (b) 300–500 hPa RH in ERA5 (1979–2020); (c) HIRS satellite UTH (1979–2020) and (d) Microwave satellite UTH (1998–2020). The time-latitude plots (left) depict % RH or UTH anomalies relative to 1995–2014 while zonal mean trends (right) apply for the respective record lengths with ±2 standard error on the calculated observed trends (dashed lines in (b–d), right panels).

Tropical ocean near-surface relative humidity in ERA5 decreases by more than 1% from 1979 to 2015 and to a lesser extent in the HadISDH-ERA5 blend. This is at odds with *amip* simulations which display a slight increase and small year to year variability in anomalies of order 0.5% RH (Figure 6c). An increase in ocean surface RH is consistent with physical expectations in which slower warming over ocean than land drives increases in surface stability (Richter & Xie, 2008). The declining observed surface relative humidity is less pronounced than ERA5-only data but consistent with a negative trend in HadISDH minus *amip* water vapor anomaly difference for the region of observational coverage (Figure S6c in Supporting Information S1); these changes are dominated by tropical oceans where accounting for measurement and reporting biases and ship height inhomogeneity is a challenge (Willett et al., 2020) and merits investigation in future work. A declining surface RH trend over tropical land is also evident (Figure 7c) though the discrepancy with *amip* simulations is less apparent, in part due to larger month to month variability. There is generally good agreement across data sets of RH variability throughout the troposphere, including the upper troposphere based on correlations between MW and AIRS ($r = 0.83$), HIRS with AIRS ($r = 0.69$) and ERA5 with AIRS ($r = 0.92$) over the 2003–2015 period.

A strong dipole in latitude-mean RH anomalies coincides with the mature phase of the 1983 and 1998 El Niño events with positive anomalies at 15°N and negative equatorial anomalies (Figure 8). Monthly RH variability appears largest in ERA5, consistent with the tropical time series in Figures 6 and 7. Smaller variability is expected for the *amip* ensemble mean, which averages out internal atmospheric variability. The HIRS infrared and MW UTH records also display smaller magnitude and consistent variability.
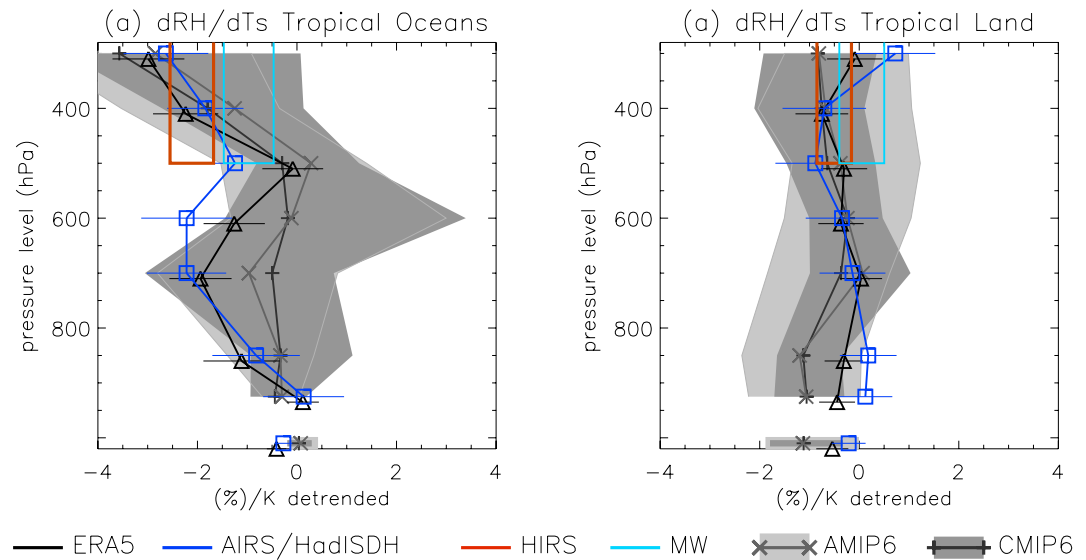
Figure 9. Detrended linear regression between relative humidity and surface temperature (*dRH/dTs*) with pressure level and at the surface for tropical (a) oceans and (b) land over 1988–2014 for *amip* and CMIP *historical* model experiments, ERA5 and HadISDH surface observations, AIRS satellite observations (2002–2014, horizontal lines depict 90% confidence range) and upper tropospheric humidity estimates from infra-red (HIRS, 1988–2014) and microwave (MW, from 1999) satellite estimates (90% confidence ranges).

Variability in ERA5 300–500 hPa RH is characterized by negative tropical anomalies and positive high latitude anomalies before ∼2002 (Figure 8b) and this explains positive tropical and negative high latitude trends greater in magnitude than 0.5% RH per decade that are not apparent in other data sets (Figure 8). This possible discontinuity could relate to the introduction of AMSU microwave instruments into ERA5 after 1998 (Hersbach et al., 2020). There is an indication of negative RH trends up to −0.5%/decade at around 40°S in *amip* and *historical* experiments (1979–2014) and HIRS (1979–2020) observations (Figure 8, right panels). Reductions in subtropical humidity have been linked with expansion of the Hadley circulation with greenhouse gas induced warming (Lau & Kim, 2015), though observed drying is weak and restricted to the poleward edge of the southern winter-hemispheric dry belt in infrared measurements (Tivig et al., 2020) and are not present in the MW record since 1999 (Figure 8d).

Finally, the sensitivity of RH throughout the tropical troposphere to interannual variability in surface temperature (from HadCRUT5) is estimated based on detrended linear regression (Figure 9). RH generally decreases with warming over interannual time-scales apart from near the surface in AIRS and HadISDH-ERA5 data. The response of RH to interannual temperature variability is generally small (0 to −2%/K) over land in all data sets. Near-surface relative humidity decreases over tropical land in warmer years in model simulations (∼−1%/K) and ERA5 (∼−0.5%/K) but not in HadISDH observations. Upper tropospheric RH tends to decrease with warming over tropical oceans at around −1 to −3%/K. AIRS and ERA5 also depict a drying in response to warming at around 700 hPa which is not reproduced by the *amip* or *historical* simulations. Overall, the response of relative humidity to interannual variability and long term warming is small in relation to its effect on the radiative feedbacks (Forster et al., 2021). Therefore, the combined temperature lapse rate and specific humidity feedback dominate, strongly amplifying climate change (trapping ∼1.3 Wm⁻² more heat for each K of warming).

4. Conclusions

Global changes in tropospheric water vapor since 1979 are assessed across a range of observations, a reanalysis, and climate model simulations. The main conclusions are:

1. Increases in moisture since 1979 are identified throughout the troposphere across multiple data sets and simulations. Global-mean column integrated water vapor increased by 1%/decade during 1988–2014 in microwave satellite observations and atmosphere-only *amip* simulations. Combined with an observed global surface

warming trend of 0.17 K/decade, this equates to global moisture increases with warming of ∼6%/K, close to, but slightly lower than, that expected from the Clausius Clapeyron equation. Tropospheric moisture increases are consistent with a strongly amplifying water vapor feedback in agreement with previous work (Colman & Soden, 2021; Forster et al., 2021; Soden et al., 2005).

2. Coupled climate model *historical* simulations overestimate 1988–2014 water vapor trends by up to a factor of two compared with *amip* simulations and some of the observations-based data sets. This is partly explained by observed internal variability which suppressed warming, and therefore also moistening rates, during the 1998–2012 period (Kosaka & Xie, 2013; Mitchell et al., 2020), though the realism of radiative forcings, the pattern of warming and climate sensitivity also play a role (Forster et al., 2021).

3. Increases in global mean 2 m specific humidity from 1988 to 2014 in *amip* simulations (∼0.8%/decade) are inconsistent with the HadISDH observations and the ERA5 reanalysis. For ERA5, this discrepancy is coincident with declining column integrated water vapor over the tropical oceans before 1993 that is inconsistent with SSM/I and SMMR microwave satellite measurements and *amip* simulations and partly explained by inhomogeneities in the observing system (Allan et al., 2020; Hersbach et al., 2020). Longer term decreases in near-surface water vapor over the Southern Hemisphere in HadISDH (1979–2014) are at odds with the ERA5 reanalysis and simulations. HadISDH also does not display near-surface relative humidity decreases over tropical land in warmer years shown in model simulations (∼−1%/K) and ERA5 (∼−0.5%/K) and as expected from drier El Niño conditions over tropical land (Trenberth & Shea, 2005). Caution is therefore required in interpreting an apparent underestimate in relative humidity decline over land by simulations compared to HadISDH (Dunn et al., 2017).

4. Robust increases in upper tropospheric water vapor over time, of around 2% per decade at 400 hPa in *amip* simulations and ERA5, are larger than lower tropospheric %/decade moisture changes. This is well understood based on the Clausius Clapeyron temperature dependence of moisture response to warming and amplified atmospheric warming aloft due to radiative convective balance, particularly over tropical oceans (Held & Soden, 2006; Ohmura, 2012). This is consistent with small changes in upper tropospheric relative humidity from satellite observations, which strengthens past assessments (e.g., Soden et al., 2005). Increases in upper tropospheric water vapor since 2002 in the AIRS satellite observations are weaker than ERA5 and model simulations.

5. Global mean near-surface water vapor increases by about 5% per K increase in surface temperature over interannual time-scales across all data sets. A larger sensitivity of 10%–15% increase in 300 hPa water vapor per K increase in surface temperature is primarily related to changes over the tropical ocean and explained by thermodynamic amplification of upper tropospheric temperature changes and the Clausius Clapeyron temperature dependence of saturation vapor pressure, as known from previous work (Dessler et al., 2008; Held & Soden, 2006). These responses are not apparent for land over interannual times-scales with temperature lapse rate increases for warmer years and %/K moisture responses similar in magnitude to the surface. AIRS satellite measurements since 2002 appear to underestimate the 600–700 hPa water vapor responses to surface temperature and this is dominated by tropical ocean relative humidity variability.

6. Climate models with larger upper tropospheric temperature changes also simulate stronger upper tropospheric water vapor changes. The range of warming rates reflect internal climate variability which dominates coupled model water vapor responses and trends over time periods less than 30 yr. This is not the case for corresponding uncoupled SST-constrained *amip* simulations where differences in tropospheric temperature and moisture responses relate more directly to the model parametrizations and merits further analysis. The MRI-ESM2 model simulates the smallest water vapor responses to observed (*amip*) surface temperature variability (3.2%/K at the surface, 6.2% per K surface temperature change at 400 hPa) while the CNRM models simulate among the largest responses (>4%/K at the surface, >11% per K surface temperature change at 400 hPa), partly explained by the stronger interannual tropospheric temperature responses to surface warming in the CNRM simulations. The CNRM models also simulate a relatively dry near-surface layer compared to other models, though similar to observation-based estimates, and weaker than ensemble average trends in near surface water vapor. This underlines the contrasting behavior between interannual and multi-decadal responses and between lower and higher altitudes.

In summary, tropospheric water vapor changes at the global scale since 1979 are consistent with a powerfully amplifying water vapor feedback based on observations-based products and the latest CMIP6 climate model simulations, as anticipated from a strong physical basis and multiple lines of evidence (Colman & Soden, 2021;

Forster et al., 2021). Discrepancies in moisture trends across data sets are strongly influenced by tropical ocean relative humidity. These trends are susceptible to inhomogeneities in the observational records that also determine unrealistic global-scale responses represented by reanalysis products such as ERA5. Future improvements in these records will further aid the evaluation and improvement of model parametrizations and coupled behavior compared to the real world.

Data Availability Statement

The HadISDH data set (Willett et al., 2014) is available from https://www.metoffice.gov.uk/hadobs/hadisdh/ and the HadCRUH data set (Willett et al., 2008) from https://www.metoffice.gov.uk/hadobs/hadcruh. ERA5 data (Hersbach et al., 2020) was extracted from https://cds.climate.copernicus.eu/. CMIP6 climate model data sets (Eyring et al., 2016) and AIRS OBS4MIP data (Tian & Hearty, 2020) were extracted from https://esgf-node.llnl.gov/search/cmip6/. The AIRS-only L3 v7 data set (AIRS Project, 2020) was extracted from https://disc.gsfc.nasa.gov/datasets/AIRS3STM_7.0/summary. SSM/I and SSMIS data (Wentz, 1997) are available from https://www.remss.com/missions/ssmi/. The HIRS UTH data (Shi & Bates, 2011) was processed from NOAA NCEI Channel 12 brightness data available from https://www.ncei.noaa.gov/products/climate-data-records/hirs-ch12-brightness-temperature. The AMSU-B and MHS microwave brightness temperature data (Chung et al., 2013) is available from https://www.avl.class.noaa.gov/. SMMR data (REMSS, 1995) was retrieved from the JPL DAAC https://podaac.jpl.nasa.gov/dataset/WENTZ_NIMBUS-7_SMMR_L2. Data were processed using Climate Data Operators (CDO) software (version 1.9.5; Schulzweida, 2021).

References

Adler, R. F., Gu, G., Wang, J.-J., Huffman, G. J., Curtis, S., & Bolvin, D. (2008). Relationships between global precipitation and surface temperature on interannual and longer time-scales (1979–2006). *Journal of Geophysical Research*, *113*, D22104. https://doi.org/10.1029/2008JD010536

AIRS Project. (2020). Aqua/AIRS L3 Monthly Standard Physical Retrieval (AIRS-only) 1 degree x 1 degree V7.0. [Dataset]. NASA Goddard Earth Sciences Data and Information Services Center. Retrieved from https://disc.gsfc.nasa.gov/datacollection/AIRS3STM_7.0.html

Allan, R. P. (2012). The role of water vapor in Earth's energy flows. *Surveys in Geophysics*, *33*, 557–564. https://doi.org/10.1007/s10712-011-9157-8

Allan, R. P., Barlow, M., Byrne, M. P., Cherchi, A., Douville, H., Fowler, H. J., et al. (2020). Advances in understanding large-scale responses of the water cycle to climate change. *Annals of the New York Academy of Sciences*, *1472*(1), 49–75. https://doi.org/10.1111/nyas.14337

Allan, R. P., Ramaswamy, V., & Slingo, A. (2002). A diagnostic analysis of atmospheric moisture and clear-sky radiative feedback in the Hadley Centre and Geophysical Fluid Dynamics Laboratory (GFDL) climate models. *Journal of Geophysical Research*, *4329*. https://doi.org/10.1029/2001JD001131

Allan, R. P., Ringer, M. A., & Slingo, A. (2003). Evaluation of moisture in the Hadley Centre climate model using simulations of HIRS water-vapor channel radiances. *Quarterly Journal of the Royal Meteorological Society*, *129*, 3371–3389. https://doi.org/10.1256/qj.02.217

Allan, R. P., & Soden, B. J. (2008). Atmospheric warming and the amplification of precipitation extremes. *Science*, *321*, 1481–1484. https://doi.org/10.1126/science.1160787

Andrews, M. B., Ridley, J. K., Wood, R. A., Andrews, T., Blockley, E. W., Booth, B., et al. (2020). Historical simulations with HadGEM3-GC3.1 for CMIP6. *Journal of Advances in Modeling Earth Systems*, *12*(6), e2019MS001995. https://doi.org/10.1029/2019MS001995

Boucher, O., Servonnat, J., Albright, A. L., Aumont, O., Balkanski, Y., Bastrikov, V., et al. (2020). Presentation and evaluation of the IPSL-CM6A-LR climate model. *Journal of Advances in Modeling Earth Systems*, *12*(7), e2019MS002010. https://doi.org/10.1029/2019MS002010

Chung, E.-S., Soden, B. J., & John, V. O. (2013). Intercalibrating microwave satellite observations for monitoring long term variations in upper- and midtropospheric water vapor. *Journal of Atmospheric and Oceanic Technology*, *30*(10), 2303–2319. https://doi.org/10.1175/JTECH-D-13-00001.1

Colman, R., & Soden, B. J. (2021). Water vapor and lapse rate feedbacks in the climate system. *Reviews of Modern Physics*, *93*(4). https://doi.org/10.1103/revmodphys.93.045002

Dessler, A. E., Schoeberl, M. R., Wang, T., Davis, S. M., & Rosenlof, K. H. (2013). Stratospheric water vapor feedback. *Proceedings of the National Academy of Sciences of the United States of America*, *110*(45), 18087–18091. https://doi.org/10.1073/pnas.1310344110

Dessler, A. E., Zhang, Z., & Yang, P. (2008). Water-vapor climate feedback inferred from climate fluctuations, 2003–2008. *Geophysical Research Letters*, *35*(20). https://doi.org/10.1029/2008gl035333

Douville, H., Raghavan, K., Renwick, J., Allan, R. P., Arias, P. A., Barlow, M., et al. (2021). Water cycle changes. In V. Masson-Delmotte, P. Zhai, A. Pirani, S. L. Connors, C. Péan, S. Berger, et al. (Eds.), *Climate change 2021: The physical science basis. Contribution of Working Group I to the Sixth Assessment Report of the Intergovernmental Panel on Climate Change*. Cambridge University Press. https://doi.org/10.1017/9781009157896.010

Dufour, A., Zolina, O., & Gulev, S. K. (2016). Atmospheric moisture transport to the Arctic: Assessment of reanalyses and analysis of transport components. *Journal of Climate*, *29*(14), 5061–5081. https://doi.org/10.1175/JCLI-D-15-0559.1

Dunn, R. J. H., Willett, K. M., Ciavarella, A., & Stott, P. A. (2017). Comparison of land surface humidity between observations and CMIP5 models. *Earth System Dynamics*, *8*(3), 719–747. https://doi.org/10.5194/esd-8-719-2017

Elsaesser, G. S., Genio, A. D. D., Jiang, J. H., & van Lier-Walqui, M. (2017). An improved convective ice parameterization for the NASA GISS Global Climate Model and impacts on cloud ice simulation. *Journal of Climate*, *30*(1), 317–336. https://doi.org/10.1175/JCLI-D-16-0346.1

Eyring, V., Bony, S., Meehl, G. A., Senior, C. A., Stevens, B., Stouffer, R. J., & Taylor, K. E. (2016). Overview of the Coupled Model Intercomparison Project Phase 6 (CMIP6) experimental design and organization. *Geoscientific Model Development*, *9*(5), 1937–1958. https://doi.org/10.5194/gmd-9-1937-2016.5194/gmd-9-1937-2016

Eyring, V., Gillett, N. P., Rao, K. M. A., Barimalala, R., Parrillo, M. B., Bellouin, N., et al. (2021). Human influence on the climate system. In V. Masson-Delmotte, P. Zhai, A. Pirani, S. L. Connors, C. Péan, S. Berger, et al. (Eds.), *Climate change 2021: The physical science basis. Contribution of Working Group I to the Sixth Assessment Report of the Intergovernmental Panel on Climate Change*. Cambridge University Press. https://doi.org/10.1017/9781009157896.005

Forster, P., Storelvmo, T., Armour, K., Collins, W., Dufresne, J. L., Frame, D., et al. (2021). The Earth's energy budget, climate feedbacks, and climate sensitivity. In V. Masson-Delmotte, P. Zhai, A. Pirani, S. L. Connors, C. Péan, S. Berger, et al. (Eds.), *Climate change 2021: The physical science basis. Contribution of Working Group I to the Sixth Assessment Report of the Intergovernmental Panel on Climate Change*. Cambridge University Press. https://doi.org/10.1017/9781009157896.009

Fowler, H. J., Lenderink, G., Prein, A. F., Westra, S., Allan, R. P., Ban, N., et al. (2021). Anthropogenic intensification of short-duration rainfall extremes. *Nature Reviews Earth & Environment*, *2*(2), 107–122. https://doi.org/10.1038/s43017-020-00128-6

Gettelman, A., Hannay, C., Bacmeister, J. T., Neale, R. B., Pendergrass, A. G., Danabasoglu, G., et al. (2019). High climate sensitivity in the Community Earth System Model Version 2 (CESM2). *Geophysical Research Letters*, *46*(14), 8329–8337. https://doi.org/10.1029/2019GL083978

He, J., Brogniez, H., & Picon, L. (2022). Evaluation of tropical water vapor from CMIP6 GCMs using the ESA CCI "water vapor" climate data records. *Atmospheric Chemistry and Physics Discussions*. https://doi.org/10.5194/acp-2021-976

Held, I. M., & Soden, B. J. (2006). Robust responses of the hydrological cycle to global warming. *Journal of Climate*, *19*, 5686–5699. https://doi.org/10.1175/JCLI3990.1

Hersbach, H., Bell, B., Berrisford, P., Hirahara, S., Horányi, A., Muñoz-Sabater, J., et al. (2020). The ERA5 global reanalysis. *Quarterly Journal of the Royal Meteorological Society*, *146*(730), 1999–2049. https://doi.org/10.1002/qj.3803.1002/qj.3803

John, V. O., Shi, L., Chung, E. S., Allan, R. P., Buehler, S. A., & Soden, B. J. (2021). Upper tropospheric humidity. In J. Blunden & D. S. Arndt (Eds.), *State of the climate in 2020* (Vol. 102, pp. S55–S56). Cambridge University Press. https://doi.org/10.1175/BAMS-D-21-0098.1

Kosaka, Y., & Xie, S.-P. (2013). Recent global-warming hiatus tied to equatorial Pacific surface cooling. *Nature*, *501*, 403–407. https://doi.org/10.1038/nature12534

Lang, T., Naumann, A. K., Stevens, B., & Buehler, S. A. (2021). Tropical free-tropospheric humidity differences and their effect on the clear-sky radiation budget in global storm-resolving models. *Journal of Advances in Modeling Earth Systems*, *13*(11). https://doi.org/10.1029/2021MS002514

Lau, W. K. M., & Kim, K.-M. (2015). Robust Hadley circulation changes and increasing global dryness due to CO_2 warming from CMIP5 model projections. *Proceedings of the National Academy of Sciences*, *112*(12), 3630–3635. https://doi.org/10.1073/pnas.1418682112

Lovato, T., Peano, D., Butenschön, M., Materia, S., Iovino, D., Scoccimarro, E., et al. (2021). CMIP6 simulations with the CMCC Earth System Model (CMCC-ESM2). *Journal of Advances in Modeling Earth Systems*, e2021MS002814. https://doi.org/10.1029/2021MS002814

Manabe, S., & Wetherald, R. T. (1967). Thermal equilibrium of the atmosphere with a given distribution of relative humidity. *Journal of the Atmospheric Sciences*, *24*, 241–259. https://doi.org/10.1175/1520-0469(1967)024<0241:teotaw>2.0.co;2:TEOTAW%3E2.0.CO;2

McCarthy, M. P., & Toumi, R. (2004). Observed interannual variability of tropical troposphere relative humidity. *Journal of Climate*, *17*(16), 3181–3191. https://doi.org/10.1175/15200442(2004)017<3181:oivott>2.0.co;2

Mears, C. A., Wang, J., Smith, D., & Wentz, F. J. (2015). Intercomparison of total precipitable water measurements made by satellite-borne microwave radiometers and ground-based GPS instruments. *Journal of Geophysical Research: Atmospheres*, *120*(6), 2492–2504. https://doi.org/10.1002/2014jd022694

Mitchell, D. M., Lo, Y. E., Seviour, W. J., Haimberger, L., & Polvani, L. M. (2020). The vertical profile of recent tropical temperature trends: Persistent model biases in the context of internal variability. *Environmental Research Letters*, *15*(10), 1040b4. https://doi.org/10.1088/1748-9326/ab9af7

Morice, C. P., Kennedy, J. J., Rayner, N. A., Winn, J. P., Hogan, E., Killick, R. E., et al. (2021). An updated assessment of near-surface temperature change from 1850: The HadCRUT5 data set. *Journal of Geophysical Research: Atmospheres*, *126*(3), e2019JD032361. https://doi.org/10.1029/2019JD032361

Nusbaumer, J., Alexander, P. M., LeGrande, A. N., & Tedesco, M. (2019). Spatial shift of Greenland moisture sources related to enhanced Arctic warming. *Geophysical Research Letters*, *46*(24), 14723–14731. https://doi.org/10.1029/2019GL084633

Nygård, T., Naakka, T., & Vihma, T. (2020). Horizontal moisture transport dominates the regional moistening patterns in the Arctic. *Journal of Climate*, *33*(16), 6793–6807. https://doi.org/10.1175/JCLI-D-19-0891.1

Ohmura, A. (2012). Enhanced temperature variability in high-altitude climate change. *Theoretical and Applied Climatology*, *110*(4), 499–508. https://doi.org/10.1007/s00704-012-0687-x

REMSS. (1995). NIMBUS-7 SMMR GLOBAL AIR-SEA PARAMETERS IN SWATH (Wentz). [Dataset]. NASA Physical Oceanography DAAC. Retrieved from http://podaac.jpl.nasa.gov/dataset/WENTZ_NIMBUS-7_SMMR_L2

Richter, I., & Xie, S. P. (2008). The muted precipitation increase in global warming simulations: A surface evaporation perspective. *Journal of Geophysical Research*, *113*, D24118. https://doi.org/10.1029/2008JD010561

Rinke, A., Segger, B., Crewell, S., Maturilli, M., Naakka, T., Nygård, T., et al. (2019). Trends of vertically integrated water vapor over the arctic during 1979–2016: Consistent moistening all over? *Journal of Climate*, *32*(18), 6097–6116. https://doi.org/10.1175/JCLI-D-19-0092.1

Santer, B. D., Po-Chedley, S., Mears, C., Fyfe, J. C., Gillett, N., Fu, Q., et al. (2021). Using climate model simulations to constrain observations. *Journal of Climate*, *34*(15), 6281–6301. https://doi.org/10.1175/JCLI-D-20-0768.1

Schröder, M., Lockhoff, M., Fell, F., Forsythe, J., Trent, T., Bennartz, R., et al. (2018). The GEWEX water vapor assessment archive of water vapor products from satellite observations and reanalyses. *Earth System Science Data*, *10*, 1093–1117. https://doi.org/10.5194/essd-10-1093-2018

Schulzweida, U. (2021). CDO User Guide. [Software]. https://doi.org/10.5281/zenodo.5614769

Scoccimarro, E., Peano, D., Gualdi, S., Bellucci, A., Lovato, T., Fogli, P. G., & Navarra, A. (2021). Extreme events representation in CMCC-CM2 high and very-high-resolution general circulation models. *Geoscientific Model Development Discussions*, *2021*, 1–18. https://doi.org/10.5194/gmd-2021-294

Séférian, R., Nabat, P., Michou, M., Saint-Martin, D., Voldoire, A., Colin, J., et al. (2019). Evaluation of CNRM Earth System Model, CNRM-ESM2-1: Role of Earth system processes in present-day and future climate. *Journal of Advances in Modeling Earth Systems*, *11*(12), 4182–4227. https://doi.org/10.1029/2019MS001791

Seland, Ø., Bentsen, M., Olivié, D., Toniazzo, T., Gjermundsen, A., Graff, L. S., et al. (2020). Overview of the Norwegian Earth System Model (NorESM2) and key climate response of CMIP6 DECK, historical, and scenario simulations. *Geoscientific Model Development*, *13*(12), 6165–6200. https://doi.org/10.5194/gmd-13-6165-2020

Shi, L., & Bates, J. J. (2011). Three decades of intersatellite-calibrated high-resolution infrared radiation sounder upper tropospheric water vapor. *Journal of Geophysical Research: Atmospheres*, *116*(D4). https://doi.org/10.1029/2010jd014847

Simmons, A. J., Poli, P., Dee, D. P., Berrisford, P., Hersbach, H., Kobayashi, S., & Peubey, C. (2014). Estimating low-frequency variability and trends in atmospheric temperature using era-interim. *Quarterly Journal of the Royal Meteorological Society*, *140*(679), 329–353. https://doi.org/10.1002/qj.2317

Simmons, A. J., Untch, A., Jakob, C., Kållberg, P., & Undén, P. (1999). Stratospheric water vapor and tropical tropopause temperatures in ECMWF analyses and multiyear simulations. *Quarterly Journal of the Royal Meteorological Society*, *125*(553), 353–386. https://doi.org/10.1002/qj.49712555318

Simmons, A. J., Willett, K. M., Jones, P. D., Thorne, P. W., & Dee, D. P. (2010). Low-frequency variations in surface atmospheric humidity, temperature, and precipitation: Inferences from reanalyses and monthly gridded observational data sets. *Journal of Geophysical Research*, *115*, D01110. https://doi.org/10.1029/2009JD012442

Soden, B. J., Jackson, D. L., Ramaswamy, V., Schwarzkopf, M. D., & Huang, X. (2005). The radiative signature of upper tropospheric moistening. *Science*, *310*, 841–844. https://doi.org/10.1126/science.1115602

Soden, B. J., Wetherald, R. T., Stenchikov, G. L., & Robock, A. (2002). Global cooling after the eruption of Mount Pinatubo: A test of climate feedback by water vapor. *Science*, *296*, 727–730. https://doi.org/10.1126/science.296.5568.727

Song, Y. H., Nashwan, M. S., Chung, E.-S., & Shahid, S. (2021). Advances in CMIP6 INM-CM5 over CMIP5 INM-CM4 for precipitation simulation in South Korea. *Atmospheric Research*, *247*, 105261. https://doi.org/10.1016/j.atmosres.2020.105261

Steiner, A. K., Ladstädter, F., Randel, W. J., Maycock, A. C., Fu, Q., Claud, C., et al. (2020). Observed temperature changes in the troposphere and stratosphere from 1979 to 2018. *Journal of Climate*, *33*(19), 8165–8194. https://doi.org/10.1175/JCLI-D-19-0998.1

Stevens, B., Sherwood, S. C., Bony, S., & Webb, M. J. (2016). Prospects for narrowing bounds on Earth's equilibrium climate sensitivity. *Earth's Future*, *4*(11), 512–522. https://doi.org/10.1002/2016EF000376

Sun, W., Lin, B., Hu, Y., Lukashin, C., Kato, S., & Liu, Z. (2011). On the consistency of ceres longwave flux and airs temperature and humidity profiles. *Journal of Geophysical Research: Atmospheres*, *116*(D17). https://doi.org/10.1029/2011JD016153

Swaminathan, R., Parker, R. J., Jones, C. G., Allan, R. P., Quaife, T., Kelley, D. I., et al. (2021). The physical climate at global warming thresholds as seen in the UK Earth System Model. *Journal of Climate*, 1–64. https://doi.org/10.1175/JCLI-D-21-0234.1

Swart, N. C., Cole, J. N. S., Kharin, V. V., Lazare, M., Scinocca, J. F., Gillett, N. P., et al. (2019). The Canadian Earth System Model version 5 (CanESM5.0.3). *Geoscientific Model Development*, *12*(11), 4823–4873. https://doi.org/10.5194/gmd-12-4823-2019

Tatebe, H., Ogura, T., Nitta, T., Komuro, Y., Ogochi, K., Takemura, T., et al. (2019). Description and basic evaluation of simulated mean state, internal variability, and climate sensitivity in MIROC6. *Geoscientific Model Development*, *12*(7), 2727–2765. https://doi.org/10.5194/gmd-12-2727-2019

Tian, B., Fetzer, E. J., & Manning, E. M. (2019). The atmospheric infrared sounder Obs4MIPs version 2 data set. *Earth and Space Science*, *6*(2), 324–333. https://doi.org/10.1029/2018EA000508

Tian, B., & Hearty, T. (2020). Estimating and removing the sampling biases of the AIRS Obs4MIPs V2 data. *Earth and Space Science*, *7*(12), e2020EA001438. https://doi.org/10.1029/2020EA001438

Tivig, M., Grützun, V., John, V. O., & Buehler, S. A. (2020). Trends in upper-tropospheric humidity: Expansion of the subtropical dry zones? *Journal of Climate*, *33*(6), 2149–2161. https://doi.org/10.1175/JCLI-D-19-0046.1

Trenberth, K. E., & Shea, D. J. (2005). Relationships between precipitation and surface temperature. *Geophysical Research Letters*, *32*(14), L14703. https://doi.org/10.1029/2005GL022760

Trent, T., Schröder, M., & Remedios, J. (2019). GEWEX water vapor assessment: Validation of AIRS tropospheric humidity profiles with characterized radiosonde soundings. *Journal of Geophysical Research: Atmospheres*, *124*(2), 886–906. https://doi.org/10.1029/2018JD028930

Voldoire, A., Saint-Martin, D., Sénési, S., Decharme, B., Alias, A., Chevallier, M., et al. (2019). Evaluation of CMIP6 DECK experiments with CNRM-CM6-1. *Journal of Advances in Modeling Earth Systems*, *11*(7), 2177–2213. https://doi.org/10.1029/2019MS001683

Wentz, F. J. (1997). A well-calibrated ocean algorithm for sensor microwave/imager. *Journal of Geophysical Research*, *102*(C4), 8703–8718. https://doi.org/10.1029/96JC01751

Wentz, F. J. (2015). A 17 yr climate record of environmental parameters derived from the Tropical Rainfall Measuring Mission (TRMM) microwave imager. *Journal of Climate*, *28*(17), 6882–6902. https://doi.org/10.1175/jcli-d-15-0155.1

Wentz, F. J., & Francis, E. A. (1992). Nimbus-7 SMMR ocean products, 1979–1984 (Technical Report). Remote Sensing Systems Technical Report 033192 [Available from Remote Sensing Systems, 1101 College Ave., Santa Rosa, CA 95404]. [Dataset]. https://podaac.jpl.nasa.gov/dataset/WENTZNIMBUS-7SMMRL2

Willett, K. M., Dunn, R. J. H., Kennedy, J. J., & Berry, D. I. (2020). Development of the HadISDH marine humidity climate monitoring data set. *Earth System Science Data*, *12*(4), 2853–2880. https://doi.org/10.5194/essd-12-2853-2020

Willett, K. M., Dunn, R. J. H., Thorne, P. W., Bell, S., de Podesta, M., Parker, D. E., et al. (2014). HadISDH land surface multi-variable humidity and temperature record for climate monitoring. *Climate of the Past*, *10*(6), 1983–2006. https://doi.org/10.5194/cp-10-1983-2014

Willett, K. M., Jones, P. D., Gillett, N. P., & Thorne, P. W. (2008). Recent changes in surface humidity: Development of the HadCRUH data set. *Journal of Climate*, *21*(20), 5364–5383. https://doi.org/10.1175/2008JCLI2274.1

Wu, T., Lu, Y., Fang, Y., Xin, X., Li, L., Li, W., et al. (2019). The Beijing Climate Center Climate System Model (BCC-CSM): The main progress from CMIP5 to CMIP6. *Geoscientific Model Development*, *12*(4), 1573–1600. https://doi.org/10.5194/gmd-12-1573-2019

Yukimoto, S., Kawai, H., Koshiro, T., Oshima, N., Yoshida, K., Urakawa, S., et al. (2019). The Meteorological Research Institute Earth System Model Version 2.0, MRI-ESM2.0: Description and basic evaluation of the physical component. *Journal of the Meteorological Society of Japan. Series II*, *97*(5), 931–965. https://doi.org/10.2151/jmsj.2019-051

Zhao, M., Golaz, J.-C., Held, I. M., Guo, H., Balaji, V., Benson, R., et al. (2018). The GFDL global atmosphere and land model AM4.0/LM4.0: 1. Simulation characteristics with prescribed SSTs. *Journal of Advances in Modeling Earth Systems*, *10*(3), 691–734. https://doi.org/10.1002/2017MS001208

Ziehn, T., Chamberlain, M. A., Law, R. M., Lenton, A., Bodman, R. W., Dix, M., et al. (2020). The Australian Earth System Model: ACCESS-ESM1.5. *Journal of Southern Hemisphere Earth Systems Science*, *70*(1), 193. https://doi.org/10.1071/es19035